ÇUKUROVA UNIVERSITY
INSTITUTE OF NATURAL AND APPLIED SCIENCES

MSc THESIS

Hüsnü EĞİTMEN

FLOW MEASUREMENTS AROUND A BIO-INSPIRED BLUFF BODY

DEPARTMENT OF MECHANICAL ENGINEERING

ADANA-2021

ABSTRACT

MSc THESIS

FLOW MEASUREMENTS AROUND A BIO-INSPIRED BLUFF BODY

Hüsnü EĞİTMEN

ÇUKUROVA UNIVERSITY
INSTITUTE OF NATURAL AND APPLIED SCIENCES
DEPARTMENT OF MECHANICAL ENGINEERING

Supervisor : Asst. Prof. Dr. Göktürk Memduh ÖZKAN
Year: 2021, Pages: 75
Juries : Asst. Prof. Dr. Göktürk Memduh ÖZKAN
: Prof. Dr. Hüseyin AKILLI
: Asst. Prof. Dr. Erhan FIRAT

The aim of the present study is to design an aero/hydro dynamically efficient bluff body inspired by the denticles of the fastest shark; *Isurus oxyrinchus*. A novel shape is developed utilizing the real scales of the denticle presented by the available literature. Experiments were carried out in a water tunnel using the Particle image velocimetry technique to obtain the velocity field around the body. In order to understand and compare the aero/hydrodynamic characteristics of the bio-inspired bluff body (bio-body), one of the most studied bluff body shape, i.e. a circular cylinder was involved for all considered parameters. The bio-body was printed using Polylactic Acid (PLA+) as the raw material whereas the circular cylinder was made of smooth Plexiglas. Since the flow around the novel bio-body is highly three-dimensional, various planes and sections were considered for PIV measurements. The evaluated results showed that the bio-body has better aero/hydrodynamic properties compared with the circular cylinder. The features that prove better aero/hydrodynamic characteristics of bio-body over the cylinder are: (I) The reduction of Reynolds stresses in all velocity components; (II) the shrinking of vortex formation length and lessening of turbulence intensity; (III) the eliminated vibrations in the near wake region. It is believed that this study introduces a new inspiration to the bluff body designs in various engineering applications such as unmanned underwater vehicles, submarines, ship hulls, etc.

Keywords: biomimicry, denticle, shark skin, PIV, bluff body, cylinder

ÖZ

YÜKSEK LİSANS TEZİ

BİO-İLHAMLI BİR KÜT CİSİM ETRAFINDAKİ AKIŞ ÖLÇÜMLERİ

Hüsnü EĞİTMEN

ÇUKUROVA ÜNİVERSİTESİ
FEN BİLİMLERİ ENSTİTÜSÜ
MAKİNE MÜHENDİSLİĞİ ANABİLİM DALI

Danışman : Dr.Öğr. Üyesi Göktürk Memduh ÖZKAN
Yıl: 2021, Sayfa: 75
Jüri : Dr.Öğr. Üyesi Göktürk Memduh ÖZKAN
: Prof. Dr. Hüseyin AKILLI
: Dr.Öğr. Üyesi Erhan FIRAT

Bu çalışmanın amacı, en hızlı köpekbalığı olan *Isurus oxyrinchus'un* diş benzeri çıkıntılarından esinlenerek, aero-hidrodinamik olarak etkili bir küt cisim geliştirmektir. Mevcut literatür tarafından sunulan diş benzeri pulların gerçek ölçekleri kullanılarak yeni bir geometri geliştirilmiştir. Deneyler, cisim etrafındaki hız alanını elde etmek için parçacık görüntü hız ölçüm tekniği kullanılarak bir su tünelinde gerçekleştirilmiştir. Biyo- ilhamlı küt cismin (biyo-cisim) aero/hidrodinamik karakterini anlamak ve karşılaştırmak için, en çok çalışılan küt cisim şekillerinden biri olan dairesel bir silindir, ele alınan tüm parametreler için çalışmaya dâhil edilmiştir. Biyo-cisim, hammadde olarak Polilaktik asit (PLA+) kullanılarak, dairesel silindir ise pürüzsüz pleksiglastan üretilmiştir. Yeni biyo-cisim etrafındaki akış yüksek oranda üç boyutlu olduğundan, PIV ölçümleri için çeşitli düzlemler ve kesitler dikkate alınmıştır. Değerlendirilen sonuçlar, biyo-cismin dairesel silindire kıyasla daha iyi aero/hidrodinamik özelliklere sahip olduğunu göstermiştir. Biyo-cismin silindire kıyasla daha iyi aero/hidrodinamik özelliklerini kanıtlayan özellikler şunlardır: (I) Tüm hız bileşenleri için azalmış Reynolds gerilmeleri; (II) daralan girdap oluşum uzunluğu ve daha düşük türbülans şiddeti; (III) yakın art izi bölgesinde titreşimlerin yok olması. Bu çalışmanın, insansız sualtı araçları, denizaltılar, gemi gövdeleri vb. çeşitli mühendislik uygulamaları için, küt cisim tasarımlarına yeni bir ilham kaynağı sunacağına inanılmaktadır.

Anahtar Kelimeler: Dişbenzeri yapı, köpek balığı derisi, aerodinamik/hidrodinamik, PIV, küt cisim, silindir.

EXTENDED SUMMARY

Inventions inspired by nature and biological living things are called biomimicry. Modifications on bluff-body shapes can be a good example in this sense which are replicated utilizing the flying and swimming animals. Some examples are; the modification of an airfoil inspired by a dragonfly (Shi, et al., 2012), sinusoidal leading edge airfoil inspired from humpback whales for improving the maneuverability (Post et al.,2018), and modification of trailing edge inspired from night owl because of its silent flight (Bodling & Sharma, 2019). Furthermore, shark skin has been one of the focused bio-inspiration field chosen as the major issue of this project because of its role in reducing friction drag. Shortfin mako, also known as Isurus oxyrinchus, is the fastest swimming shark among the others. It is estimated that it can approach to a speed of 40 m/s (Motta et al., 2012), making its skin very useful in biomimicry for improving the aerodynamic/hydrodynamic design of vehicles.

All kinds of vehicles are directly affected by drag coefficient in terms of fuel efficiency, and one of the biggest reasons for high drag coefficient is the wrong design of the body. In order to obtain a low drag coefficient, the vehicle has to be aerodynamically/hydrodynamically designed. Consequently, analyzing new bluff bodies that are spearheading new designs and contributing to scientific research is important.

The skin of sharks has a tooth-like denticles in the streamwise direction that form grooves and channels that pull water towards the shark and push it across its body, eliminating resistance, enabling drag reduction, and fast swimming. This shark skin structure has become an interesting field since it has promised better performance. Moreover, this tooth-like structure (called riblet) has a skin friction reduction effect in a turbulent flow. The varying configuration of this riblet structure which are inspired from shark skin is still under investigation of many resaerchers and up to 9.9% drag reduction is reported by Bechert et al.,1997. On

the other side, the effect of 3-D printed scaled denticles attached on an airfoil's leading edge is investigated by Domel et al.,2018a who revealed that the denticles can delay the stall angle by the effect of generated spanwise vortices from the denticles.

This project aims to obtain a new type of aero-hydrodynamic bluff-body design inspired by sharkskin denticle. The flow structure and turbulent flow charactristics were analyzed utilizing Particle Image Velocimetry. For all cases, Reynolds stresses were reduced compared to the cylinder. The maximum obtained percent reduction was 71.1%, 88.4%, and 77% for streamwise Reynolds normal stress, transverse Reynolds normal stress, and Reynolds shear stresses, respectively. Moreover, compared to the cylinder, lessening of turbulence intensity and the shrinking of vortex formation length were observed. FFT results reveal that, unlike the cylinder, the contour of the bio-body does not cause vibration in the near wake region. It is believed that this developed bio-body will be novel model for future design considerations since it presented better aero-hydrodynamic flow features according to the presented results.

GENİŞLETİLMİŞ ÖZET

Yapılan birçok yeni buluşlar doğadan ve biyolojik canlılardan esinlenilerek icat edilmiştir .Günümüze kadar biyomimikri aracılığıyla küt cisimler üzerinde şekil bakımından birçok değişiklikler yapılmış ve yapılan bu değişikliklerin etkisi araştırılmıştır . Bunlara örnek olarak ; uçuş sırasında süzülme yeteneği ve her yönden hızlanabilme özelliği nedeni ile yusufcuktan esinlenilerek kanat üzerinde yapılan değişiklikler (SHI ve diğerleri,2012), manevra kabiliyeti nedeni ile kambur balinaların yüzgecinden esinlenerek kanatın hücum kenarının sinüzoidal şekilindeki modifikasyonu (Post ve diğerleri,2018) veya sessiz uçuşu nedeni ile gece kuşunun kuyruk kısmından ilham alınarak kanadın kuyruk tarafında titreşimini azaltmak için yapılan değişiklikler gösterilebilir (Bodling and Sharma,2019). Bunlara ilaveten köpek balıklarının deri yapısı da araştırılanlar arasında bulunmaktadır. *Isurus oxyrinchus* olarak adlandırılan sivriburun camgöz köpekbalıkları diğer köpekbalıkları arasından en hızlı yüzen köpekbalıklardır.Bu köpek balığı türünün hızının 40m/s'ye kadar çıkabileceği düşünülmektedir (Motto ve diğerleri,2012). Verilen bu bilgiler ışığında ve proje kapsamı içerisinde daha iyi aerodinamik/hidrodinamik tasarım elde edilebileceği düşünülmektedir.

Köpek balığının deri yapısı; yüzme sırasında direnci azaltmaya yarayan, akış yönünde oluk ve küçük kanallardan oluşan diş benzeri çıkıntılara sahiptir. Bu oluklu yapılar daha iyi performans vaat ettiği için araştırmacılar tarafından büyük bir ilgi odağı haline gelmiştir. Köpek balığının deri yapısından ilham alınan oluklu yapı bir çok konfigürasyonda incelenmiş ve 9.9%'a kadar sürtünmede azalma gözlenmiştir (Bechert ve diğerleri,1997). Öte yandan, bir kanat profilinin hücum kenarı üzerine tutturulmuş üç boyutlu diş benzeri çıkıntıların etkisi, diş benzeri çıkıntılardan üretilen boylamasına girdapların etkisi ile durma açısını geciktirebileceğini ortaya koyan Domel ve ark.(2018a) tarafından incelenmiştir.

Bu proje, köpek balığı derisinden ilham alınarak, yeni bir aero-hidrodinamik küt cisim tasarımı elde etmeyi amaçlamaktadır. Akış yapısı ve türbülanslı akış özellikleri Parçacık Görüntü Hız Ölçüm Tekniği (PIV) kullanılarak analiz edilmiştir. Sunulan sonuçlara göre, ele alınan tüm durumlarda, Reynolds gerilmeleri silindire kıyasla azalmıştır. Elde edilen maksimum yüzde azalma miktarları, akış yönünde ve akışa dik yönde Reynolds normal gerilmeleri ve Reynolds kayma gerilmeleri için sırasıyla 71.1%, 88.4% ve 77% oranlarında elde edilmiştir. Ayrıca, silindir ile karşılaştırıldığında, türbülans şiddetinin azaldığı ve girdap oluşum uzunluğunun daraldığı gözlenmiştir. FFT sonuçları, silindirin aksine, biyo-cismin konturunun yakın art izi bölgesinde titreşime neden olmadığını ortaya koymaktadır. Geliştirilen biyo-cismin daha iyi aero-hidrodinamik akış özellikleri sunması nedeniyle gelecekteki tasarım parametreleri için yeni bir model olacağına inanılmaktadır.

ACKNOWLEDGEMENT

First and foremost, praise and thanks to God, the Almighty, for His showers of blessings throughout my research work to complete the research. I would like to express my deep and sincere gratitude to my research supervisor, Assist. Prof. Dr Gokturk M. Ozkan and Head, Centre for Mechanical Engineering, Çukurova University, for allowing me to do research and providing invaluable guidance throughout this research. His dynamism, vision, sincerity and motivation have deeply inspired me. He has taught me the methodology to carry out the research and present the research works as clearly as possible. It was a great privilege and honor to work and study under his guidance. I am extremely grateful for what he has offered me. I would also like to thank him for his friendship, empathy, and a great sense of humor. I am extending my heartfelt thanks to his wife, family for their acceptance and patience during the discussion I had with him on research work and thesis preparation. I would also like to thank Prof. Dr Hüseyin AKILLI for his support and encouragement.

I would like to thank Beşir ŞAHİN for sharing their suggestions and knowledge with me.

I sincerely thank Research Assistant Sergen TÜMSE, Project Assistant Mehmet Oğuz TAŞCI, Research Assistant Hurrem AKBIYIK, Research Assistant İbrahim DİKER and Laboratory technician Sefa MERAL for their help during my experiments.

CONTENTS **PAGE**

LIST OF FIGURES PAGE

NOMENCLATURE

PIV : Particle Image Velocimetry
Bio-body : Bio-inspired bluff body
RMS : Root-Mean-Square
LIF : Laser-induced fluorescence
f_v : Vortex formation frequency
DNS : Direct Numerical Simulations
LES : Large Eddy Simulation
VIV : Vortex-Induced Vibration
ϕ_s : Flow separation angle of the cylinder
$C_{L,rms}$: Root-Mean-Square of lift coefficient
β : Porosity value
θ : Plate angle
D_s : Shroud Diameter
DR : Drag reduction
s^+ : Wall units
s : Peak to peak space of riblets
u_t : Friction velocity
v : Kinematic viscosity
l_g+ : Non-dimensionalized groove area
A_g : Groove cross-section area
ESEM : Environmental scanning electron microscope
AOA : Angle of attack
ds : Particle separation
IA : Interrogation area
d_{IntWin} : Interrogation window size of IA.
ω : Time-averaged vorticity

FOV	: Field of view
Ψ	: Streamline topology
St	: Strouhal number
f	: Dominant shedding frequency
L_r	: Recirculation length
F1	: First focal point of vortices
F2	: Second focal point of vortices
S	: Saddle point
D	: Cylinder diameter
Dh	: Hydraulic diameter of bio-body
AR	: Aspect ratio
U_∞	: Free-stream velocity
$<\omega D/ U^2_\infty >$	: Normalized-time averaged vorticity
u	: Time-averaged Streamwise velocity
u'	: Fluctuation velocity in the streamwise direction
v	: Transverse velocity
v'	: Fluctuation velocity in the transverse direction
$<u'u'>$	: streamwise Reynold normal stress
$<v'v'>$	: transverse Reynold normal stress
$<u'v'>$	: Normalized Reynold shear stress
$<u'u'>_{max}/U^2_\infty$,	: The peak value of the streamwise Reynold normal stress
$<v'v'>_{max}/U^2_\infty$,	: The peak value of the transverse Reynold normal stress

1. INTRODUCTION

Bodies exposed to fluid flow are classified as either streamlined or blunt, according to their overall shape. A body that is shaped according to envisaged streamlines in the fluid flow, is called a streamlined body. Streamlined bodies such as bullet and airfoil seem as contoured and smooth. On the other hand, blunt or bluff bodies tend to block the flow. The streamlined bodies travel through the fluid flow much more effortless than bluff or blunt bodies, and this is why streamlining is crucial for the design of vehicles and aero planes.

Bio inspiration from nature and flow around bluff-body have a similar place in the sense of better hydrodynamic/aerodynamic characteristics. Flow over the bluff bodies (Gabbai&Benaroya,2005) is a common event relevant to flow behavior when it comes across an obstacle. Circumfluent flow around an airplane wing, automobile, bridge, underwater vehicle, tower block and an unmanned aerial vehicle can be given as examples of the flow over an obstacle (Bhushan, 2009; Choi et al., 2008). In general, bluff bodies are subjected to high speed flows so that the pressure drag is more effective than skin friction drag on the total drag coefficient. When Reynolds number approaches to a critical value, vortex shedding occurs in the bluff body's wake region, leading to the pressure drop, called pressure drag. This phenomenon is valid for a wide range of Reynolds numbers (Choi et al., 2008).

Vortex shedding generates vibrations, called vortex-induced vibrations (VIV’s) on the bluff body. VIV’s can cause resonance and consequent catastrophic failures on the structures. Therefore, prevention or attenuation of vortex shedding in the near wake of a bluff body has been studied over decades. In addition to flow control techniques, streamlined body shapes' design plays a vital role in preventing the vortex shedding mechanism. This can also enhance the fuel consumption of vehicles used in transportation, contributing to the reduction of greenhouse gases. Many various types of research were conducted to understand the vortex shedding phenomena better. Scientists have managed to implement morphological changes inspired by nature with well-studied geometries to control the adverse effects of VIV's by obtaining better aero-hydro dynamic characteristics..

1.1. Flow Over a Circular Cylinder

Numerous researches have been conducted using a circular cylinder to reveal the basic flow characteristics over bluff bodies. This is due to the tempting simplicity of setting an experimental facility to measure flow quantities in the wake of circular cylinders. Figure1.1 presents the visualization of flow over a cylinder by Williamson & Govardhan (2004) who investigated different flow regimes downstream of a cylinder. They reported that the flow is involved with the detachment of boundary layer and following shedding of vortices resulting in the oscillations of the flow after a critical Reynolds number. The resultant flow structure corresponds to a periodic motion in the wake of the body. This periodic motion and structure evolved by the vortex shedding are called as famous von Karman Vortex Street. The vortex shedding with a discrete frequency can cause structural vibrations, leading to structural failures on huge constructions such as bridges and high-rise buildings.

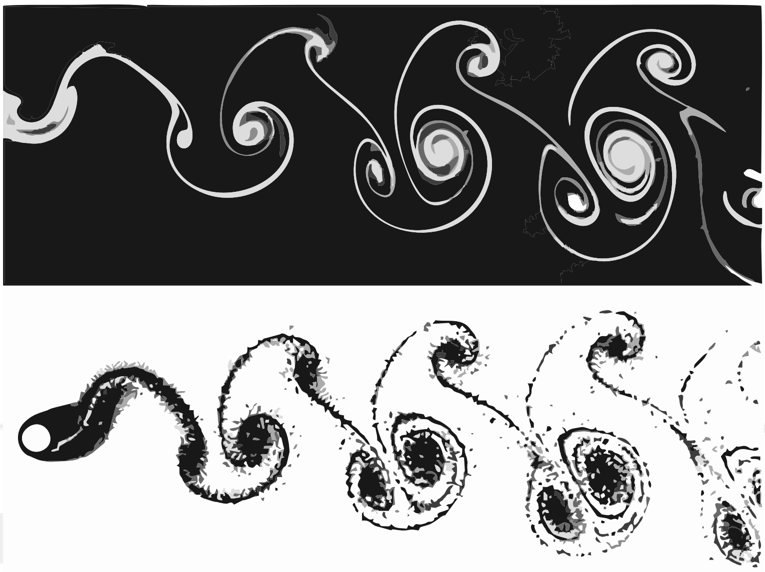

Figure 1.1. Dye visualization images of Williamson & Govardhan (2004) in the laminar flow regime ($Re_D < 200$)

1.1.1. Flow Separation

Rigid objects travelling through a fluid or vice versa develop a boundary layer. The boundary layer can either be laminar or turbulent, depending on the Reynolds number. Flow separation or boundary layer separation can be noticed when the fluid can no longer follow the body's profile and start to detach from the surface. The fluid travels far enough through the adverse pressure gradient so that the boundary layer's speed relative to the body becomes zero and the fluid starts flowing in the reverse direction, namely, separation occurs.

Separation causes an increase in the pressure drag because of the pressure differences between the from and the rear stagnation points of the cylinder; for this reason, researches are still being conducted to design more aero/hydro dynamic bodies to decrease pressure differences (Basu 1985&1986).

1.1.2. Wake

The roll up of separated shear layers into the wake is responsible for the formation of a wake. Wakes are characterized by high shear stresses within low velocity regions along the wake's centerline, in addition to the high velocity regions along the edges of shear layers (see Figure 1.2). Viscous stress and vorticity are considered to be the dominant characteristics in the wakes. The boundary layer detached from the bluff body to form the first free shear layers enveloping a relatively slow recirculation region is called as the near wake. The shedding of the vortices may seem at a distinct frequency. However, at relatively high Reynolds numbers, it may occur so fiercely to generate an irregular turbulent flow in this region called turbulent wake.

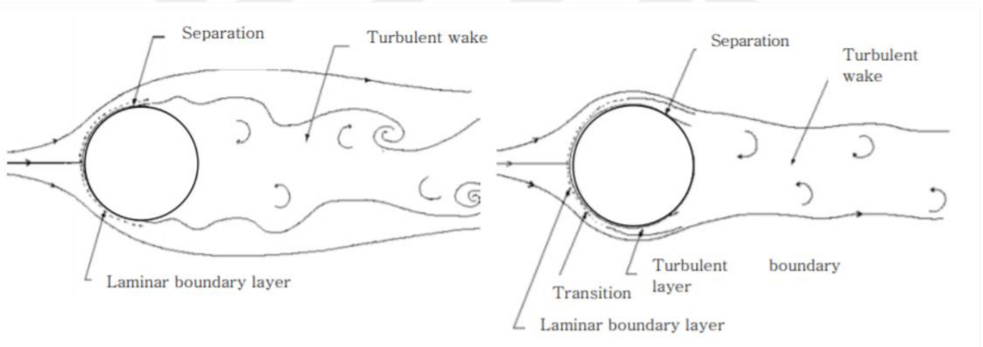

Figure 1.2. The wake sub-critical (left) and super-critical (right) flow around a circular cylinder (Merrick & Bitsuamlak, 2008).

1.1.3. Biomimetic in engineering applications

Biomimetic allows mimicking the biology and nature to develop nanomaterials, Nano devices, and processes as a multidisciplinary field. The biological properties such as the morphology have been utilized to develop beneficial engineering outcomes, e.g., hydrophobic and self-cleaning surfaces, drag reduction, and aerodynamic performance enhancement. Inspiration from biologically living creatures and non-living stuff from nature is called ‘biomimetic’. Biomimetic is derived from the Greek word biomimesis. Otto Schmitt brought up the word biomimetic by mimicking electrical nerve actions in 1957 (Bushan,2009). A large number of objects including aquatic animals, seashells, bacteria, plants and land animals with functions and interest area are shown in Figure1.3.

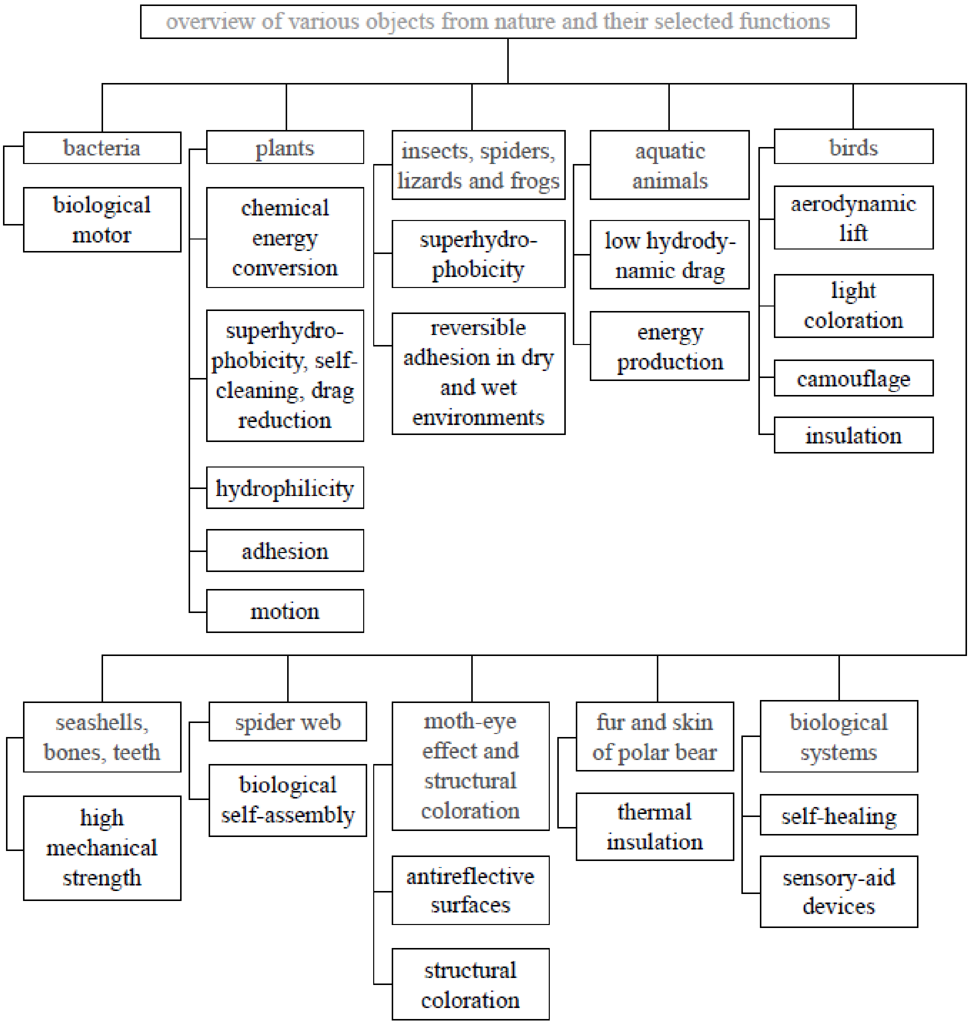

Figure 1.3. Various objects observed from nature and their functions of interest (Bhushan, 2009).

This study aims designing a bio-inspired bluff body (bio-body) utilizing the shape of denticles on the fastest shark in nature: *Isurus oxyrinchus* (Domel et al.,2018a; Motta et al. 2012; Wen et al., 2015). Planar PIV measurements were performed around the bio-body and critical flow features are revealed to understand this newly developed bluff body's flow structure

2. LITERATURE SURVEY

2.1. Cylinder As A Bluff Body

Various researches were conducted to understand the flow characteristics around a circular cylinder for different Reynolds number regimes, as one of the earliest works, Griffin and Ramberg (1974) studied the spacing of vortices in the wake region of a lateral vibrating circular cylinder for Re_D = 144 and Re_D =190. An inverse relationship between initial circulation (K) and the vortex formation length (l_F) obtained for oscillations up to half of the cylinder’s diameter. The strength and spacing ratio obtained by satisfying a minimum-error criterion. They found that the vortex street’s lateral spacing decreases as the amplitude of the vibration on the cylinder increases. Besides, they found that if the frequency does not change, the lengthwise spacing remains constant.

A review by Basu (1985&1986) has discussed the influence of turbulence, the effect of surface roughness on Strouhal number, drag coefficient, and root mean square (RMS) of the lift coefficient around a circular cylinder. They revealed that small scale turbulence possibly creates the fluctuating lift force. Also, he investigates the relation between pressure fluctuation across the bluff body due to shedding phenomena and separation angle and found that vortex shedding causes pressure fluctuations around the bluff body.

Park Cheol-Woo and Lee Sang-Joon (2000) investigated the free end effect of circular cylinders with various aspect ratios (L/D=6,10,13). They conducted the experiments in a subsonic wind tunnel and used hotwire anemometer for velocity measurements at Re_D= 20000. They also measured the mean pressure distributions along the cylinder. The results reveal that the shedding frequency decreases and vortex formation length increase with decreasing aspect ratio.

Apart from these studies, Summer et al. (2005) studied flow characteristics of two staggered circular cylinders with different pitch ratios (1.125 to 4) and varying incidence angles from 0^o to 90^o. They performed experiments in a wind tunnel to measure the mean aerodynamic forces and vortex shedding frequencies for Re_D=3.2x10^4 to 7.4 x 10^4. They examined the results in three sections; (I) *P/D*<1.5 (closely spaced), (ii) 1.5≤*P/D*≤2.5 (moderately spaced), and (iii)*P/D*>2.5 (widely spaced). They showed that the aerodynamic forces significantly vary with incidence angle for small pitch ratios (1.125-1.25); however, the flow patterns are found to be similar to those in a single bluff body. At moderate pitch ratios (1.5-2.5), they noticed that flow patterns change with incidence angles and sudden appearance or disappearance of the periodic vortex shedding occurs at small angles. Finally, they found that two cylinders act like two individual cylinders for high pitch ratios, and both of them undergo Von Karman vortex shedding for all incidence angles.

Rostamy et al. (2012) studied the flow structure around a finite circular cylinder. The cylinder is placed in a turbulent boundary layer of a flat plate where the ratio of boundary layer thickness to cylinder diameter is *δ/D*=1.6. Different aspect ratios (*AR*=3.0, 5.7, 9.0) used throughout the experiments. They conducted experiments in a low-speed wind tunnel via employing Particle Image Velocimetry. They reported that the reattachment of the flow is dependent on the aspect ratio of the cylinder. The reattachment position took place at *x/D*=0.25 , *x/D*=0.21, *x/D*=0.3, *x/D*= 0.29 for *AR*=9,*AR*=7, *AR*=5 and *AR*=3 respectively. Moreover, they found that the time-averaged vortices at the free end extend beyond the cylinder as the aspect ratio decreases.

An extensive review, including more study about the circular cylinder, triangular cylinder, square cylinder, and rectangular cylinder with various flow regimes, was studied by Derakhshandeh and Alam (2019).

Wang et al. (2021) studied the effect of blockage ratio on a circular cylinder, flat plate, and square cylinder flows. PIV experiments were conducted at Re_D=3200, 4600 and 5400 for four different blockage ratios (β=0.25,0.3,0.4,0.5) while keeping the wall boundary layer thickness kept about 0.35D. Based on PIV measurement results, they found that the wall restriction apt to level the flow by relieving the vortex shedding. In most cases, the vortex shedding was utterly prevented for large enough blockage ratios, and a steady flow in the wake region was observed. However, for circular cylinder between β=0.25 and β=0.33, the wall restriction found to be led to the intensification of vortex shedding. Their results also indicated that the Strouhal number increases droningly with the blockage ratio. Reynolds number in terms of alternating the wake pattern was found less significant than the blockage ratio.

Lu and Sato(1996) numerically investigated the flow structures around a rotationally oscillating cylinder with a constant angular speed. They also investigated the effect of cylinder rotation on the flow structure and the forces acting on the cylinder. The results verified with experimental results, which available in the literature. The numerical investigations made at Re_D =200,1000 and 3000 with a rotational velocity range of $0.1\leq\alpha\leq0.3$, and with an oscillating frequency (oscillating frequency of cylinder/vortex shedding frequency of cylinder) range of $0.5\leq f_e/f_o\leq4.0$. As a result of these numerical investigations, they found that the vortex formation evolution in the near wake is related to the variety of forces.

Williamson (1996) submitted a review on two-dimensional wake flow measurements, new techniques in the experimentation (laser-induced fluorescence(*LIF*) and particle-image velocimetry(*PIV*), 3D direct numerical simulations(*DNS*)) and effected on secondary stability analysis. He mentioned the importance of understanding the effects of end boundary conditions on flow over a lengthy cylinder, consequently under the influence of the end conditions. Furthermore, concerning vortex dynamics, also, Williamson mentioned that two types of dimensionality could be defined; (I) extrinsic, such as; effects due to end condition,(II) intrinsic, such as; 3-D shifting caused by natural instabilities. As concluding remarks, he touched on questions that could not find the answer yet; some of these are: The degree to which the 3-D vortex dynamics phenomena, for low Reynolds numbers, is valid for high Reynolds number flows? How do the 3-D vortex dynamics affect both the steady and the unsteady state fluid forces on a cylinder? Can we use knowledge concerning 3-D vortex dynamics flow phenomena for uniform cylinders in uniform flow in the cases of complex flows?

Apart from these studies, Mittal and Kumar (2001) employed finite element methods to investigate the flow around a stationary cylinder mounted to flexible support free to vibrate both in the streamwise and the transverse direction at a Reynolds number range $Re_D=10^3$-10^4. They concluded that flexible support movement affects vortex shedding frequency, which might cause lock-in (resonance) and the mode of vortex shedding.

Jordan (2002) investigated separated shear layers of a cylinder via implementing large eddy simulation (*LES*) methodology at subcritical flow regime (Re_D=8000) in order to gain more knowledge about shear-layer properties. As a result, power spectra show that the grid spacing resolves the equilibrium range. The shear layer interaction downstream of the circular cylinder was found similar with literature, but he could not find numerous modes as in previous studies. Moreover, he observed a narrow-band higher mode and a second broadband mode downstream of the circular cylinder within the transition process. Finally, he referred to a study made by Unal and Rockwell (1988) to remark similarities with his study.

A comprehensive review of the progress of vortex-induced vibrations (*VIVs*) around a circular cylinder was performed by Sarpkaya (2004), who discussed experimental and numerical methods available in the literature. As the result of this review, he pointed out suggestions regarding what can be studied about vortex-induced vibration. His suggestions included (I) Performing a numerical simulation of two parallel shear layers subjected to sinusoidal motion to gain better knowledge of vortex shedding modes. (II) Accomplishing both experimental measurement and numerical simulation to perceive the effect of body closeness to the test section. (III) Finding more techniques about suppressing the vortex shedding and controlling the vortex shedding phenomena.

Another extensive review, including VIV, critical mass, effective elasticity, vortex wake modes, and forced vibration on the elastically mounted cylinder were released by C.Williamson & Govardhan (2004). In conclusion, they touched on unanswered questions: What is the highest attainable vortex-induced vibration amplitude of an elastically mounted cylinder? What is the relation between peak and mass damping?. Other than this, they reviewed the assignation of peak amplitude for the laminar regime, i.e., Re<200. They pointed to new ideas obtained from CFD simulation results, such as using vorticity to measure force and precisely measure the vorticity using *PIV*.

Gabbai and Benaroya (2005) reviewed the mathematical model used for the study VIV of circular cylinders, including Wake-oscillator models, force decomposition models, and single-degree-of-freedom. As a suggestion, they suggested that researchers should focus on predicting the dynamic reaction of structures to *VIV* more precisely in the upcoming years. Furthermore, they noted challenges regarding the prediction of how each parameter of *VIV* affects the structural response individually. Besides, they said that better prediction of *VIV* could enable better vortex shedding suppression. Other than these, they state that even if passive flow control mechanisms accomplish suppression of vortex shedding, these control techniques did not eliminate the VIV; on the other hand, they underlined the promising value of active flow control techniques.

Unal and Rockwell (1988) studied controlling the vortex shedding with a splitter plate downstream of the cylinder in the range of Re_D=140-3600. They found that the splitter plate's sufficient closeness to the cylinder may eliminate the instability at low Reynolds numbers. On the other hand, they found that for large Reynolds numbers, a splitter plate restrains the large scale wake vortices'' full development but did not eliminate the instability.

Akilli et al. (2008) studied flow characteristics of a circular cylinder at Re=6300 with various splitter plate lengths (*L/D*=0.2-2.4) and thickness in a water tunnel via particle image velocimetry technique. Their experimental results concluded that the plate's thickness did not significantly affect flow patterns for *L/D*≥1.0. They also reported that prevention of the interaction of separated shear layers was accomplished with the existence of a splitter plate.

Rodriquez et al. (2015) investigated the wake region and vortex shedding phenomena of a circular cylinder for different flow regimes in the range of $Re_D=2.5\text{x}10^5$-$8.5\text{ x}10^5$ by implementing the *LES* methodology. They observed three cases, i.e. (i) one-Bubble asymmetric case, (ii) two Bubble-asymmetric case, and (iii) two-Bubble symmetric case. In the first two cases, the flow downstream of the cylinder bends towards the lower pressure side of the cylinder. At supercritical region (iii), the flow separation occurs at ϕ_s $=148^o$ with symmetric wake region and lift fluctuations found to decrease to the value of $C_{L,rms}$ ≈0.07 at the end of the subcritical regime. Moreover, the Strouhal number was found constant around St≈ 0.44.

The use of a splitter plate in vortex shedding control lead to studies of various splitter plate configurations. One of these studies was made by Ozkan et al. (2017), who investigated the effect of using a porous plate with different porosity values (β) and different plate angles (θ) on the vortex shedding suppression. They conducted experiments via particle image velocimetry system and much-used flow visualization spectroscopic method, i.e., laser-induced fluorescence. They also performed drag force measurements to understand the effect of porous plates. They revealed the porosity values of β=0.4 and 0.5 with plate angle between $35^o \leq \theta \leq 90^o$ as effective cases on vortex shedding suppression and found that porous plate led to a decrement of turbulent fluctuations for all porosity ratios for $\theta<30^o$.

2.2. Biomimetic

Firstly, it should be mentioned that many inventions have been made throughout the history of inspiration from nature and biological living things; however, only a few are listed in this study (mainly about morphological changes in existing geometries). One of the interesting subjects in biomimicry is sharkskin which is known to be effective in the reduction of skin friction. Bechert et al. (1997).

Bechert et al. (1997) investigated a surface with longitudinal ribs on drag coefficient in turbulent flow conditions. They performed in the Berlin oil channel, which has a shear stress balance with an unparalleled accuracy ±0.3%. The Reynolds number based on the channel's width varied from Re_{ch}=5000 to Re_{ch}=33000. They found that with shark skin inspired riblets, drag reductions (*DR*) up to 9.9% can be achieved for $16< s^{+} <18$ ($s+=\frac{su_t}{v}$; s is peak to peak space of riblets , u_t is friction velocity, and υ is kinematic viscosity). Figure 2.1 shows the schematic representation of sawtooth riblets.

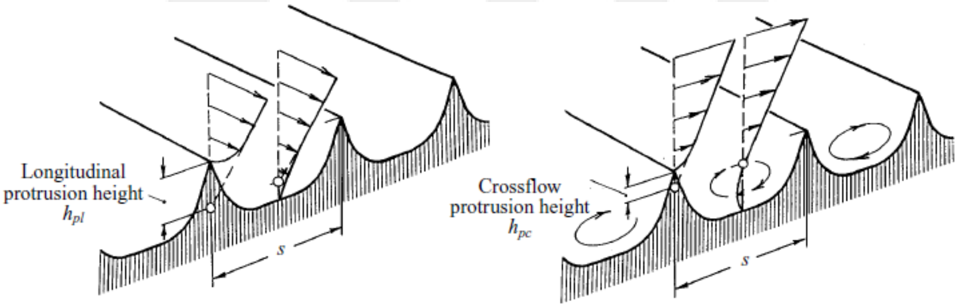

Figure 2.1. Illustration of sawtooth riblet

A comprehensive article discussed by Bechert et al. (2000) addressed the biological surfaces and their applications. To be more specific, the study touched on wall shear stress reduction of shark skin and riblets, preventing injuries of hairy surfaces, self-cleaning mechanisms of lotus leaves, and applications on aircraft. A review about flow control of fishes and swimming mammals discussed by Fish and Lauder (2006): in this review, both passive and active flow control mechanisms of fishes and swimming mammals have been entreated. Dolphin's muscle characteristics enable them to reach high velocities while maintaining a fully attached turbulent boundary layer, according to Askew & Marsh, 1997. In addition to dolphin muscles, in the sense of passive flow control, the tubercles of a humpback whale were among the review subjects. The tubercles stand out with effectiveness in delaying stall angle and increasing averaged lift coefficient without affecting the averaged drag coefficient (Miklosovic et al. 2004).

In addition to the effectiveness of the shark scales on skin friction, the sharkskin's bristles found to be also effective in reducing drag. Lang et al. (2008) investigated a possible flow control mechanism of shark bristles within the boundary layer. They implemented the spectroscopic method of laser stimulated fluorescence (*LSF*) to visualize cavity vortices within the modelled shark scales; moreover, they used digital particle image velocimetry data to investigate cavity vortex formation and boundary layer characteristics. The experimentation was carried out in a water channel, and the bristled shark skin model was positioned within a boundary layer. As a result of their experiments, more than one boundary layer control mechanism of bristled shortfin mako shark skin models emerged.

A comprehensive review about the drag reduction performance of the riblet structure in turbulent flow is published by Dean and Bushan (2010). Garcia-Mayoral and Jimenez (2011) suggested another well-accepted parameter in addition to the studies used non-dimensionalized wall unit function as the main parameter, i.e. they claimed the use of the square root of the non-dimensionalized groove area (l_g+= $\sqrt{\frac{A_g}{s^2}}$) instead of considering both s^+ (wall unit function) and h^+ (groove depth) discretely. They studied the behaviour of riblet structures for $s^+ \cong$ 10- 20 via systematic direct numerical solution with increasing riblets size. In the light of this study, they found the optimum l_g+ found in the range of 10.7±1, and DR performance found %10. Figure 2.2 shows the optimal range of s^+_{opt}, h^+_{opt} and $l^+_{g,opt}$.

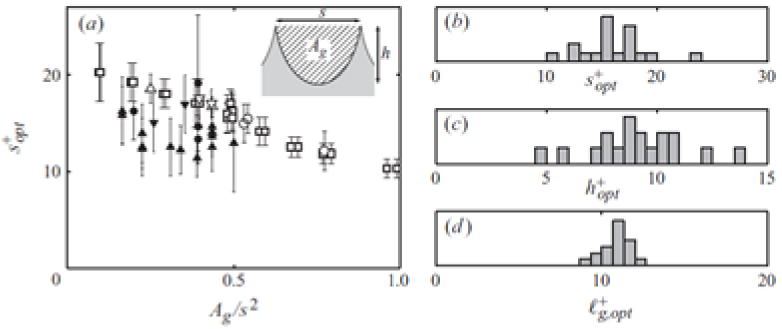

Figure 2.2. (a)Riblet spacing for maximum drag reduction, as a function of the relative groove cross-section Ag/s^2. (b–d) Histograms of the optimum performance point expressed in terms of the peak-to-peak spacing s, the groove depth h, and the square root of the groove cross-section, l_g =$\sqrt{A_g}$, for several riblet geometries (Mayoral and Jimenez, 2011)

Furthermore, other than the effect of riblet geometries on drag reduction in the turbulent boundary layer, Wen et al. (2015) studied the effect of denticle pattern and spacing on locomotion. In their study, bio-inspired solid sharkskin is manufactured as solid denticles on a flexible substrate, which enabled this artificial skin to bend freely and generate thrust via a mechanical controller's help. They considered three types of spacing arrangement: (i) staggered-overlap, (ii) linear-overlapped and (iii) linear-non-overlapped. As a result, they found that the shark-inspired denticle pattern reduced the drag at low speeds compared to the smooth surface. However, they observed an increase in drag coefficient after 25 cm·s^{-1}. Furthermore, they found that the staggered-overlapped swimming speed is increased by 25.2% over the smooth membrane. Also, they concluded that significant swimming performance assured only with the staggered-overlapped pattern.

Different from previous studies, Domel et al. (2008) investigated the denticles as a vortex generator both experimentally and numerically. The purpose of their study was to increment the aerodynamic performance of the NACA 0012 airfoil. The shortfin mako shark-inspired denticles were positioned at the suction side of NACA 0012 foil with an aspect ratio of $W/L=2.8$. The configurations of shortfin mako denticle-inspired vortex generators were obtained based upon micro-computed tomography (micro-CT) scanning of *Isurus oxyrinchus*. They identified the critical parameters that define geometric properties of denticles as (i) longitudinal length of the middle ridge denoted by l_c, (ii) longitudinal length of the side ridges denoted by l_r, (iii) latitudinal length between the outside of ridges denoted by l_s, (iv) height of the middle ridge denoted by h_1,(v) height of the side ridges denoted by h_2, (vi) tilt angle denoted by θ. During experimentation the ratios of l_c/l_s, l_c/l_r, h_1/ h_2, l_c/ h_1 were kept constant as 1.37, 1.25, 1.40, 2.95, respectively. They conducted the experiments in a water tank at Rec ≅ 4 x 104 based on chord length of NACA0012 using particle image velocimetry as the measurement method. They achieved the best aerodynamic performance of vortex generator in the lift to drag coefficient ratio for a single rowed denticle pattern with 2mm x 2mm floor space with a 0.7mm middle ridge height which was placed 26% of the chord length. Furthermore, improvement in lift to drag ratio up to 323% was achieved. As a result of this, this performance achievement is grounded on two denticle structure mechanisms; (i) denticles alter the pressure distribution along the airfoil and increase the suction. (ii) streamwise vortices created by denticles compensate for momentum loss in the boundary layer. Figure 2.3 shows the actual shape obtained from the environmental scanning electron microscope (ESEM), the designed shape of the denticle used and different configurations on the NACA0012 airfoil, together with the visualized flow around NACA0012 airfoil with denticle. In conclusion, they reported better lift-to-drag improvement compared to other commercial vortex generators even at a low angle of attack (AOA). The existence of denticle led to the formation of a separation bubble eventually an increment of suction along the cord.

Other than biomimicking of sharkskins, SHI et al. (2012) performed an experimental investigation around an airfoil inspired by a dragonfly via the Particle Image velocimetry technique. They investigate flow around both corrugated airfoil and its corresponding smooth airfoil. The experiments were conducted at Re_c=2.0x10^3 and with a variable angle of attack, i.e., AOA=0^o,4^o,$8^{o,}$ and 12^o. As a result of this study: (I) at AOA=4^o, they found corrugated airfoil delay the flow separation(II) at AOA=8^o and 12^o earlier detachment of fluid was observed, also at AOA=8^o reduction of mean lift and drag force compare to smooth airfoil was observed. (III) at AOA=12^o recirculation region reaches x/c=0.5 more away from behind the airfoil. Post et al. (2018) investigate flow around six different wing configurations inspired by humpback whales and the effect of the wings with sinusoidal leading edge on the lift. In this study, the oil film visualization and numerical methods were used to investigate these wing configurations. The experimentation was performed in a wind tunnel at various angles of attack from -2^o to 24^o within a range of Re= 10x10^5-50x10^5. They found that for sinusoidal leading-edge configurations smoothing transitions to stall regime and also delay the stall. After 16 degrees, because of its configurations, sinusoidal leading-edge models enable operation with a 25% higher lift coefficient at a higher angle of attack. The oil film visualizations reveal that flow separation occurs first behind the grooves for the sinusoidal configuration, then the head of the sinusoidal leading edges. Besides, they found that the flow across the heads alters the flow and drove the fluid flow through the grooves. In brief, the sinusoidal leading-edge configurations were found to be more effective in lift coefficient for the post-stall regimes. Bodling & Sharma(2019) performed a numerical study to understand trailing edge noise reduction of the fences. They performed large eddy simulation across both NACA0012 and night owl inspired airfoil geometry; during the computer simulations, Reynolds number based on chord length, Mach number and the AOA kept constant at Re_c=50x10^4, Ma=0.2 and AOA=0^o, respectively. They design two types of airfoil model with fences ; (I) single step and (II) stair step fence. In conclusion, they found that spectra of the surface pressure reduced at high frequencies and more or less increased at low frequency for an airfoil with fences. Also, they found that using airfoil with stair-step trailing edge enable reduction up to 10 dB in a frequency range of 500 to 5000 Hz. Moreover, the distribution of turbulence kinetic energy found further away from the trailing edge.

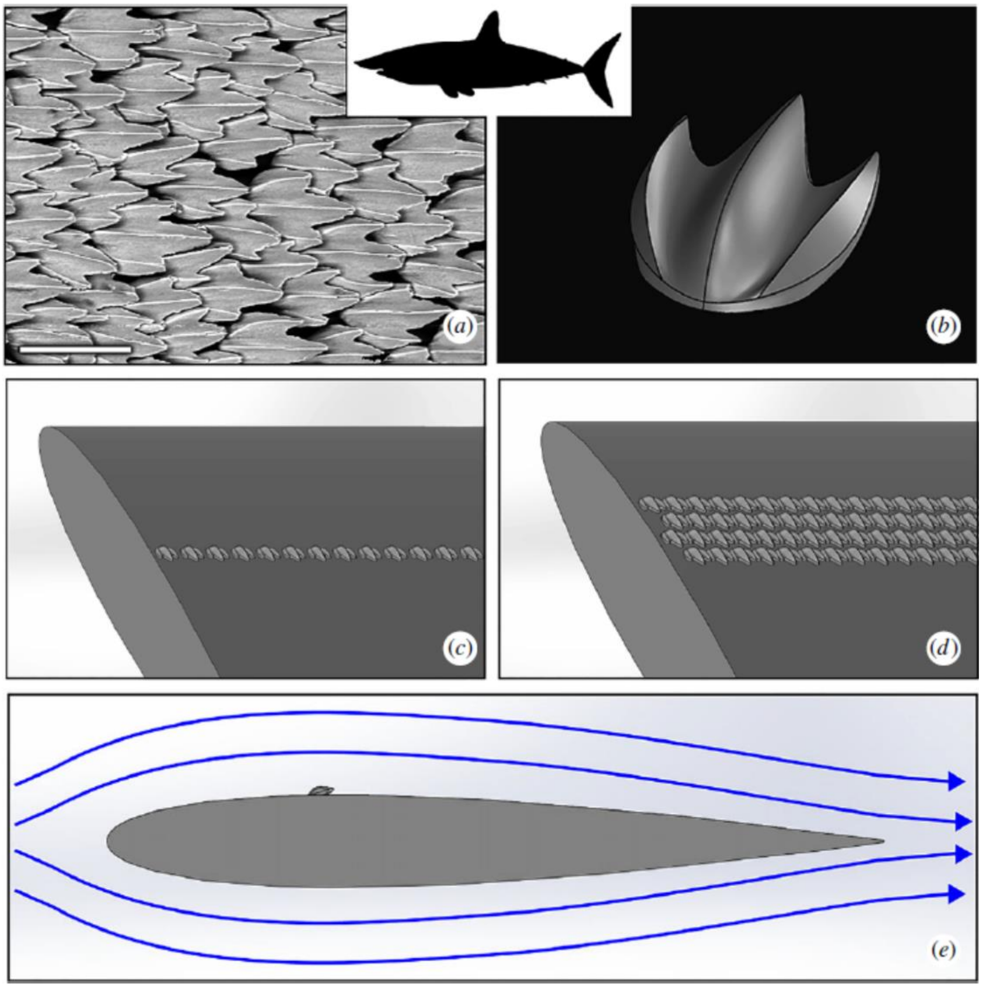

Figure 2.3. (a)shortfin mako shark image obtained from an environmental scanning electron microscope (ESEM),(b) Designed 3D denticle,(c-d) different placement on NACA0012,(e) visualized flow around NACA0012 airfoil with denticle

3. MATERIAL AND METHOD

3.1. Material

The novel Bioinspired bluff body (bio-body) was designed utilizing the geometry of skin denticles of the fastest shark in nature: *Isurus oxyrinchus*. Firstly, the primary shark scale model was redesigned using the presented features of denticles in Domel et al. (2018). The completed version of the scale model was given below in figure 3.8. Then, the model was subjected to a rescaling to satisfy geometric similarity in the original denticles shape, together with its convenience in production. The empty regions of the original denticles was filled and model's surrounding was enclosed to create the newly designed bio-body (see figure 3.9).

The models are manufactured using 3D printing technology. The bio-body was prototyped from Polylactic Acid (PLA+) material using 0.2 nozzle apparatus. Next, a thin layer of polyester paste was applied to the surface of the printed model to fill the gaps and then sanding was applied using waterproof silicon carbide paper with the size of 100µm, 200 µm, and 360 µm, respectively. Finally, acrylic paint with an emissivity coefficient of 1 $W.m^{-2}.K^{-4}$ was applied for two reasons; (i) to fill the microscopic gaps, (ii) to prevent any reflection of laser light which adversly affects the measurements.

To validate the measurements and compare the results of bio-body with one of the most studied bluff bodies in literature, a circular cylinder was also considered in this study. A D = 0.06 m circular cylinder made from plexiglass material was installed in the measurement plane which is mounded by delrin caps on both sides of the cylinder.

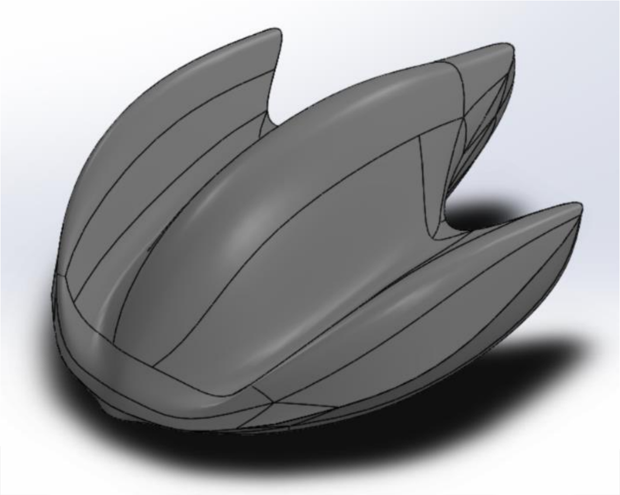

Figure 3.1. Redesigned shark scale model

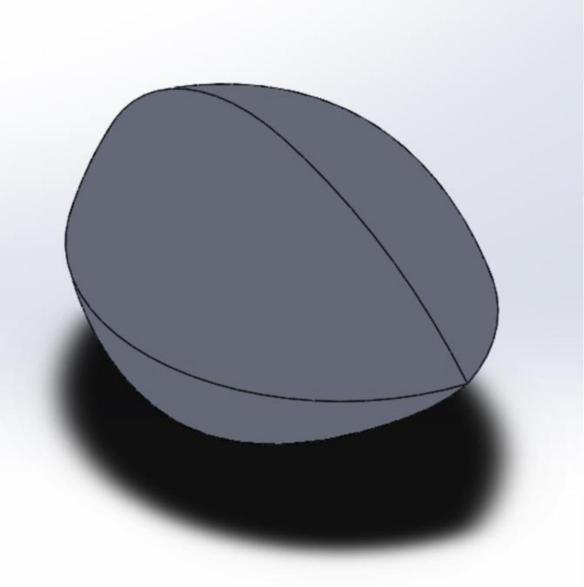

Figure 3.2. Bioinspired bluff body

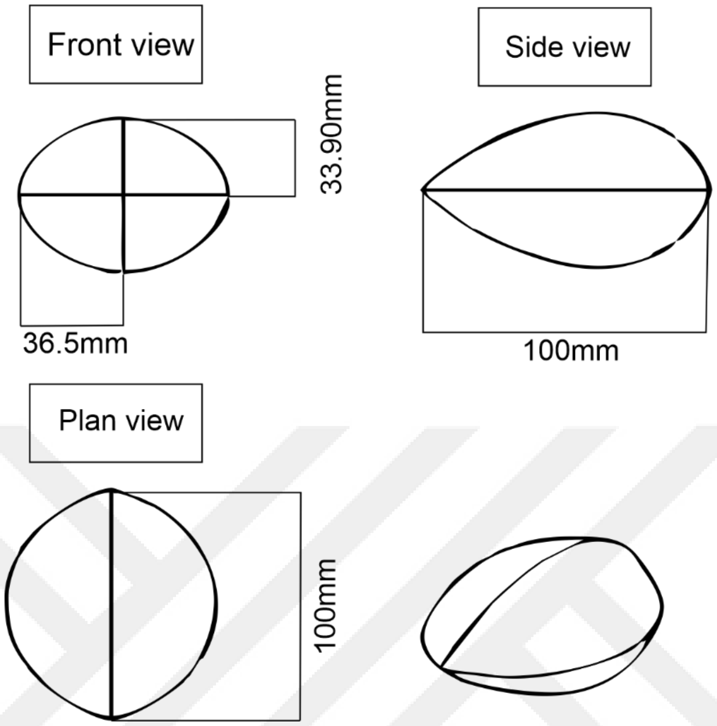

Figure 3.3. Dimensions of the bio-body

The shark scale dimension ratio was taken the same as in Domel et. al. (2018a & 2018b) i.e. l_c/l_s =1.37, l_c/l_r= 1.25, h_1/h_2 =1.40 and l_c/h_1 =2.95 (see figure 3.11). Final dimensions of the bio-body is presented in figure 3.10. where the hydraulic diameter of bio-body is calculated to be D_h = 0.068 m.

The flow structures around both bio-body and cylinder were investigated throughout the study for two Reynolds numbers. Since the flow is three-dimensional for bio-body, the experiments were conducted considering two different planes of measurements, i.e., side and plan views (middle section and the quadrant).

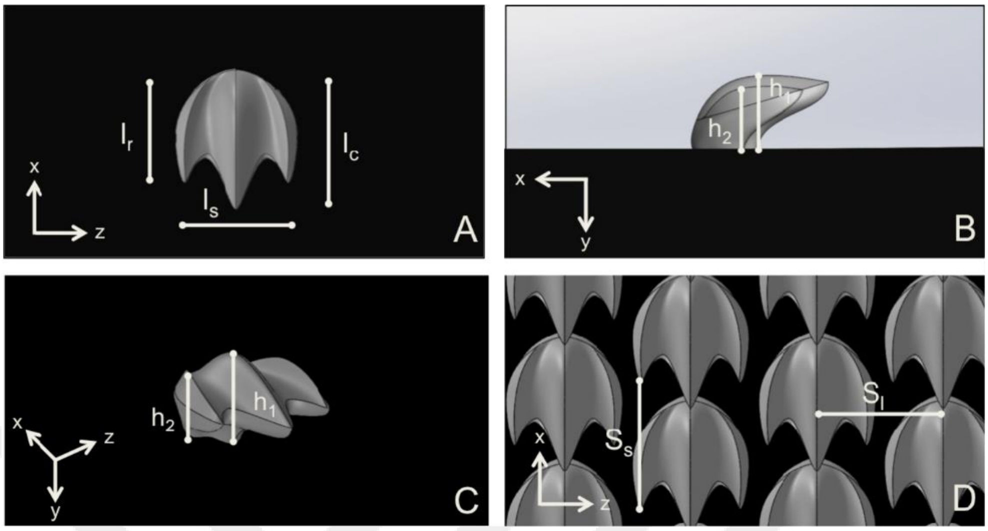

Figure 3.4. The shark denticle parameters (Domel et al. 2018b)

The experiments were carried out at 5.5 m away from the inlet of the test section. The water temperature was kept constant as T=22.7 ^{o}C corresponding to a dynamic viscosity of μ = 9.36x10^{-4} Pa.s (White,1979). Three different Reynolds numbers were considered which are calculated based on the hydraulic diameter of bio-body; Re_D= 4.45x10^3, Re_D=8.9x10^3 and Re_D=13.4x10^3. Since the flow around the bio-body dominantly three-dimensional, the velocity vector field at the midplane (centerline of the bio-body) and the quarter plane for plan view and side view were analyzed. In the coordinate system, *l* indicates the lateral distance from the centroid of the bio-body, and *h* indicates the lengthwise distance from the centroid of the bio-body.

Besides, L and H letters indicate half of the bio-body's total lateral distance and lengthwise distance, respectively. (for coordinate system and test section, see Figure 3.5).

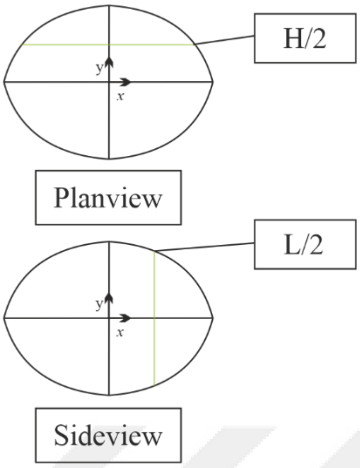

Figure 3.5. Coordinate system & and test sections

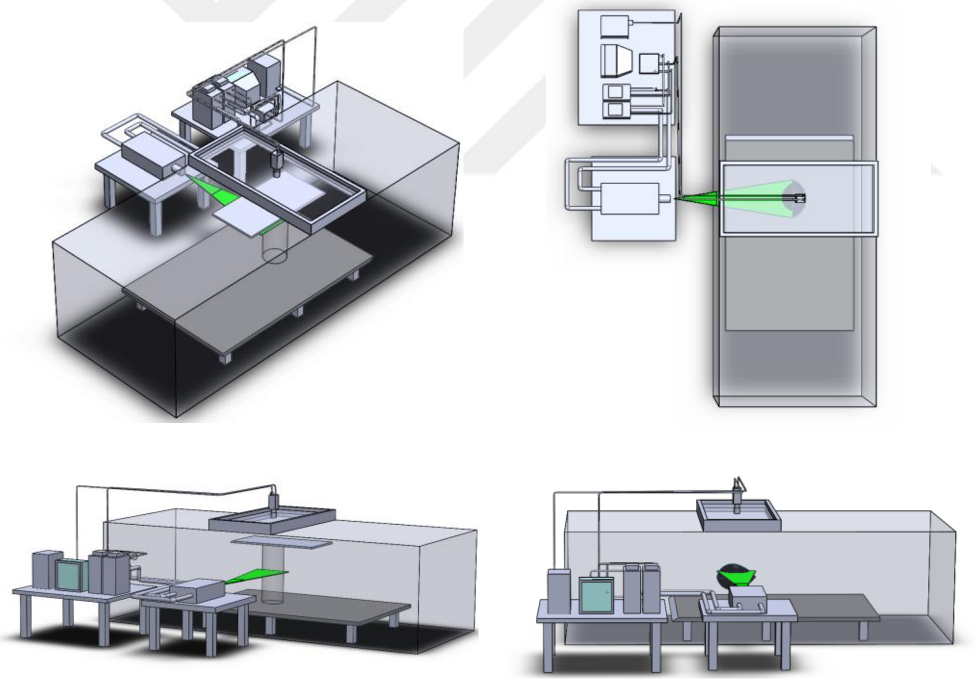

Figure 3.6. Schematic presentations of the experimental set-up

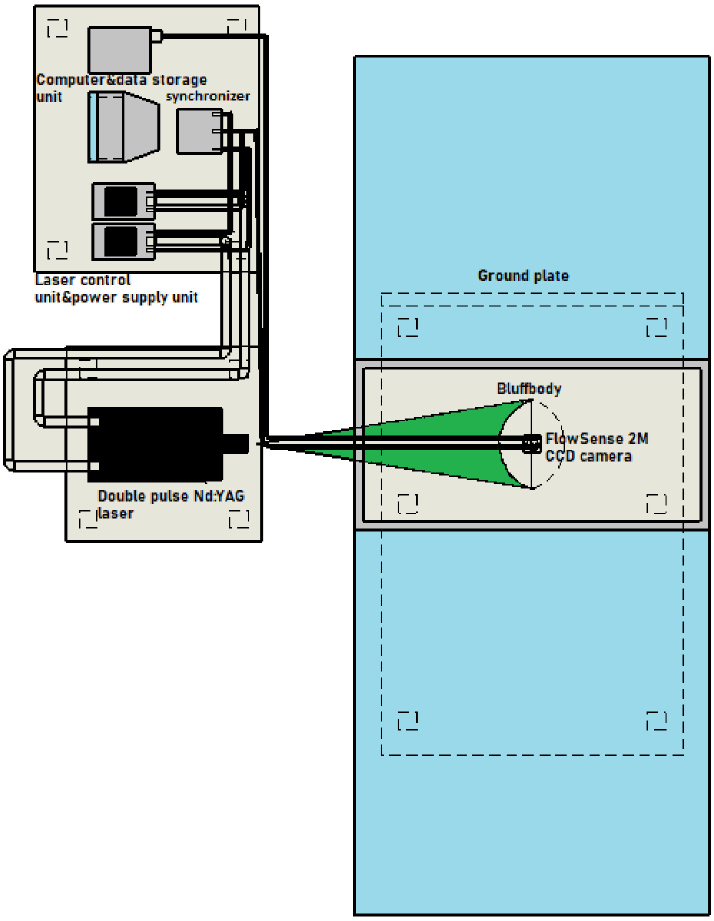

Figure 3.7. Close-up view of the experimental set-up

3.2. Experimental Method

In this study, one of the commonly used measurement techniques, i.e., Particle image velocimetry (PIV) was utilized which is an optical measurement technique that enables obtaining the velocity field in the area of interest within the entire flow region. The flow region is divided into small interrogation areas, enabling tracking the displacement of the small particles. Particle image velocimetry can be used either for flow visualization or quantitative analysis of the velocity distribution of a flow region (Lindken, R., & Burgmann, S.,2012). In order to get the velocity vector field, small tracer particles seed the flow region.

The experiments were performed in a water channel installed in the Department of Mechanical Engineering of Çukurova University. The dimensions of the water channel are 750mm × 1000mm × 8000mm (height × width × length), and it is made of 15 mm thick plexiglass (see Figure 3.3). Water is recirculated with the help of a 15 kW pump. Water supplied to the system is first filtered through sediment filters that which are capable to filter particles up to 5 µm. When the channel is filled, the pump delivers water to the test section after passing through a honeycomb to obtain uniform in the upstream. For adjusting the speed, a frequency controller unit is used. The maximum free stream velocity obtained in the channel is 0.3 m/s at a water height of $h_w = 0.55$ m.

The flow field was illuminated by a double pulsed New Wave Tempest & Gemini laser having maximum energy output of 120 mj and 532 nm wavelength. The synchronization carried out by the timer boxer enable the timing sequence between image capturing and the laser emission. The time difference between pulses arranges to ensure particle separation (d_s) stay in the range of $0.1px<d_s<0.25d_{\mathrm{IntWın}}$ for accurate peak detection (Keane, Adrian, 1990) where $d_{\mathrm{IntWın}}$ is the interrogation window size of IA. The thickness of the laser beam was adjusted as 1mm and the water was seeded with 10µm diameter spherical silver-coated particles. The image captured by a charge-coupled devices camera having a resolution of 1600x1200 pixel, a camera integrated with 60mm lens at f/4.0. The raw images were subjected to data cross-correlation algorithm to evaluate instantaneous vector fields of 1000 images so that time-averaged vector fields can be obtained. The turbulent intensity of the free-stream flow was measured to be less than 2%. Initial interrogation area of 64x64 with two refinement steps and 50% overlapped were applied, which results in 32x32 final interrogation area. The scale factor was 15.45 which corresponds to a field of view of 183mmx137mm. Experimental set up is demonstrated in figures 3.6 and 3.7.

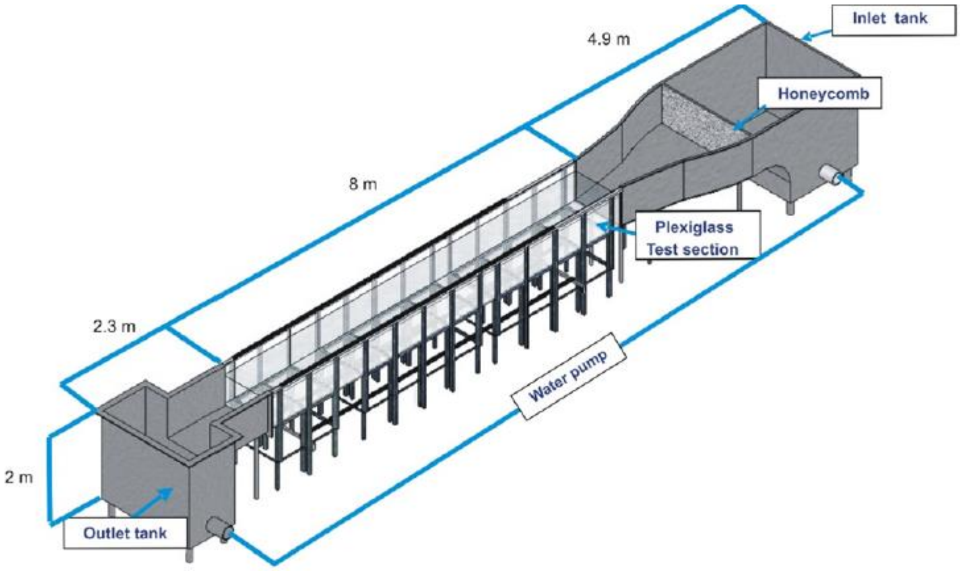

Figure 3.8. A schematic representation of the water channel.

3.2.1. Particle Image Velocimetry (PIV)

Particle Image Velocimetry is a highly preferred laser-optical method to visualize and investigate the separation of unsteady flow. The flow area is seeded with some tracer particles, periodically illuminated by a high-power laser light source, and two images are taken from the investigation region with a charged coupled device camera. Since the time interval between the displacement of the tracer particles and image capture is known, a velocity vector map in the flow field can be calculated. The PIV technique does not require any measuring probes since it provides information about the entire flow area and is advantageous over traditional techniques. The basic theory of PIV was developed many years ago, and significant

contributions made by Keane and Adrian (1991). Because of hardware restrictions, a single photo frame was exposed numerous times and analyzed using an auto-correlation technique. Images to be captured in separate frames for cross-correlation analysis were made possible due to improvements in recording speed.

The application of digital camera technology in the PIV technique at the expense of low resolution was directly recorded digitally, and the development of digital PIV settled (Westerweel 1997). Increased accuracy of PIV analysis with progress in optics, lasers, cameras, and software. Figure 3.6 demonstrates the components of the PIV system containing a computer, a laser system, a synchronizer, a CCD (Charge Coupled Device) digital camera and, a frame grabber.

3.2.2. Principles of PIV

Many technical and scientific developments require a measurement technique to measure the velocity distribution across an interrogation area of a flow field. This can be achieved by scanning a point velocity across the flow via the help of a probe, but then the instantaneous structure is lost, and only the average flow field is obtained. Flow visualization techniques can often reveal instantaneous flow structures but are only qualitative or semi-quantitative at best. An optical, non-intrusive method related to both visualization of flow and optical point techniques has developed over the last 20 years called Particle Image Velocimetry (PIV). This technique can provide a quantitative measure, including its uncertainty of the instantaneous flow velocity field of a flow field Figure 3.7 shows a general setup for the 2D PIV system**.**

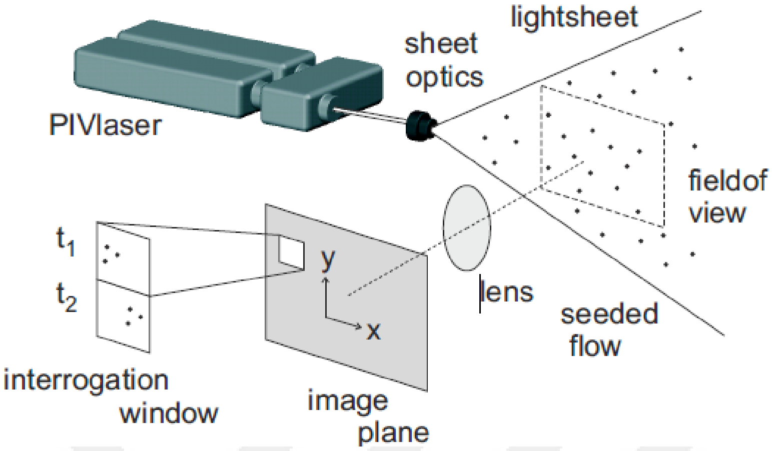

Figure 3.9. General setups of a 2D PIV system(LaVision Manual)

PIV has become an essential tool for quantitative and instantaneous measurements of laboratory flows. The flow is seeded with microscopic and buoyant particles, namely, ’tracers,’ e.g., water aerosols or oil in the air and solid particles either in flames or fluids. Recently, also Helium-filled soap bubbles have been introduced for airflow measurements. Their diameter ensures a largely more intense light scattering behaviour. A light sheet developed by passing a double pulsed laser beam through an optical arrangement with cylindrical optic lenses, the particles in the flow is illuminated twice within a very short time difference.

The particle positions at both instants of time of the laser pulses are recorded. The recorded particle displacement is measured locally by statistical means across the entire *FOV* of the images, scaled by an image magnification factor, and then divided by the known pulse separation to get velocity through the entire flow field. In most cases, a camera positioned perpendicular to the laser light sheet is shuttered to capture the light scattered from the particles. The delay between two pulses must be chosen depending on the flow velocity and the magnification factor to obtain adequate particle displacement on the CCD. Velocity vectors can be calculated from the displacement of the tracers and the time delay between the two illuminations. In order to determine images of the particles, it is assumed that the tracers follow the flow at the nearby flow velocity between the two laser illuminations. The flow field is divided into small subareas known as ‘interrogation windows.’ Using correlation techniques enables the determination of one local displacement vector within each interrogation window.

For this reason, the size of this interrogation window should be selected such that all particles within the interrogation areas have moved equally towards the same direction and at the same distance. The number of particles within each interrogation area should be at least ten for more precise results and move no more than one-quarter of the interrogation window size between the two recorded frames. Figure 3.8 shows an example of a seeded vortex.

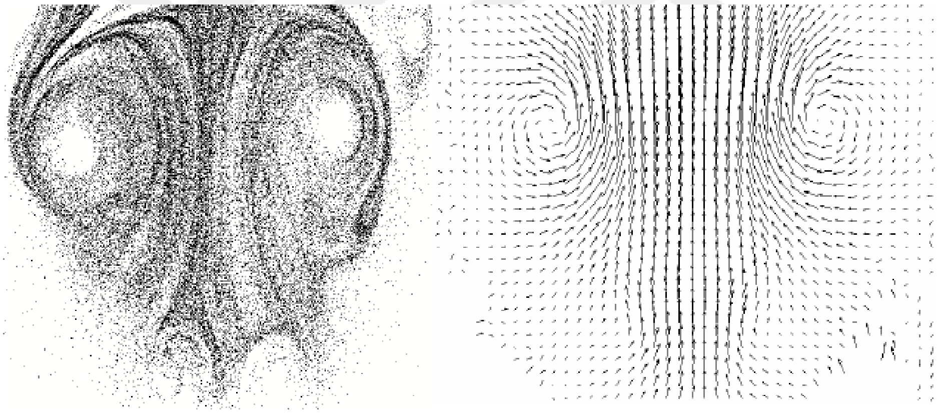

Figure 3.10. Example of a seeded vortex and flow field (LaVision Manual)

The evaluation of the particle images within each interrogation window depends on how these images are recorded. One way is to record the scattered pulsed light in one frame, namely, single frame / double exposure. These pictures can be evaluated by auto-correlation. The other way is to record the scattered light from the first pulse and the second pulse individually in a different frame. This type of recording is known as double frame / double exposure. These double-frame images can be evaluated by cross-correlation.

3.2.3. Seeding

The velocity measured in the PIV is not the flow velocity but the velocity of the dispersed tracer particles in the flow. In this context, seeding particles can be considered as real probes, and therefore seeding examinations are significant. Seeding particles should be carefully selected to add flow to monitor particle movement. The type, size, number, distribution, and tracking ability of seeding particles used in the measurements have great importance in the PIV system since these particles must travel along with the fluid, allowing them to observe the nature of the flow. These particles must have the same or approximately the same density as the used fluid; thus, they shall match the properties of the fluid. They must provide a full neutral buoyancy, and the seed particles do not alter the flow and interact with each other (Westerweel 1997). If the fluid is water, highly reflective particles need to be used for seeding the flow, such as polystyrene, fluorescent, silver-coated particles. In experiments, silver-coated particles used as seeding material. Particles are chosen according to;

- Able to track,
- Clean.
- Sufficient scatters,
- Suitably generated,
- Non-volatile, or slow to evaporate,
- Chemically inactive

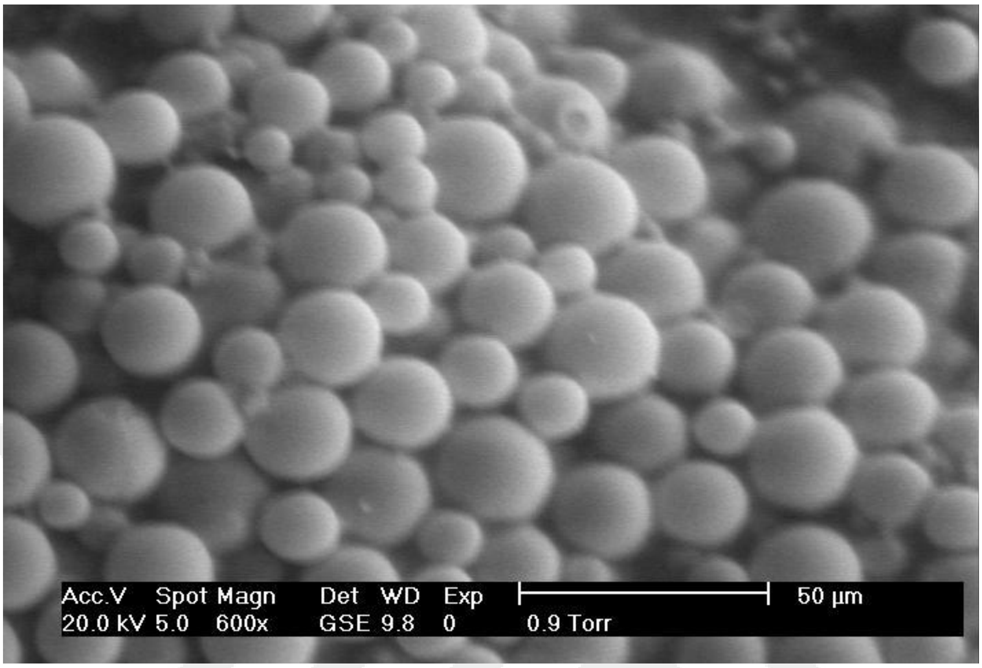

Figure 3.11. Micrograph that showing silver coated hollow glass spheres (Mayne et al. 2011)

Seeding material should be selected according to the flow to be measured and considering the current illumination system. Seeding particles should be select as large enough to reflect the light, but particles cannot follow the flow if the particle size did not choose right. The particle diameter must be the range from 0.1 to 50 µm. Therefore, tracer particles should be selected carefully to avoid inconsistencies between the particle and the flow. The number of particles also affects the accuracy of the measurements. It is crucial for obtaining a good signal peak in the cross-correlation.

3.2.3. Illumination

The illumination system is used to illuminate the flow field in the measurement area. Different techniques can be used to illuminate the area, like a pulsed laser, continuous-wave lasers and Xenon flash lambs in the PIV technique.

The measurement of particle displacement can be achieved by capturing both the initial and the end positions of the particles. The illumination technique must satisfy the following criteria:

- The time between successive light pulses should be short enough to avoid particles with an out of plane velocity component and long enough to obtain sufficient resolution images of the tracer particle’s movement.
- The light pulse duration must be short enough so that the particles do not move during exposure to prevent images from blur.
- The light should be powerful to determine the intensity of scattered light from the seeding particles and capture particles' images.

For illumination, a laser is used because of the easiness to define a laser sheet and the fact that the source is monochromatic. A solid-state Nd: YAG lasers are often used for experiments in PIV. They have high output energy, short pulse duration and emitting a wavelength of 532 nm. In this study, Nd: YAG laser is used to obtain PIV images.

3.2.4. Image Capturing

A Charge-Coupled Device (CCD) converts photons into free electrons and, images of the light scattered by the tracer particles are recorded with a Charge Coupled Device (CCD) camera via a double-pulse laser sheet. After recording the initial and final positions of tracer particles by the CCD camera, a displacement vector can be obtained.

The CCD camera, also scanned in a full-frame interline transfer stage, called a cross-correlation CCD camera, is used to obtain clear images with the time interval of the microsecond series. Full frame interline transfer progressive scan CCD camera, also called cross-correlation CCD camera, is used to obtain individual open images with a time interval of microsecond sequence. The CCD camera contains a series of detectors called pixels. There are numerous sorts of CCD cameras. Mainly, the design of the CCD array affects whether the particular camera can be used for automatic or cross-correlation image capturing. In the past, because the photographic film was used as an image capture medium, auto-correlation initially became a commonly used method of PIV image capture. Since cameras that can have a short time among double frames have been developed, cross-correlation image capture is possible. For image capture with the camera, the lighting and laser pulse must be triggered at the right time to capture their images correctly. The synchronizer is used to control all components in an accurate order.

3.2.5. Image Processing for PIV

In the PIV technique, determining the distance travelled by particles within a time between two laser pulses correlation techniques is performed. The time interval between the captured images makes possible a velocity vector to be calculated from the displacement vector.

There are three types of process methods depending on the equipment used to record the particle image records and the seed particle concentration. These are cross-correlation, auto-correlation, and particle tracking. The recorded images are divided into small sub-regions called integration areas, each containing particle images. Cross and automatic correlation processes are performed using Fast Fourier Transforms, and a speed vector map is generated with processing the image on a regular grid of small sub-regions.

The oldest PIV processing technique is auto-correlation processing. In the auto-correlation process, one single image frame is exposed several times and determined by the film-based recording system because the free particle cannot record image recordings in two closely spaced conditions over time, and it is processed on a regular grid of small sub-regions. Two single exposure image frames are recorded in cross-correlation.

The cross-correlation process divides image frames into small sub-regions, such as in auto-correlation, and a sub-region recorded in the first laser pulse is cross-correlated with a sub-region recorded in the second laser pulse. The exact direction of displacement is determined since images in image one and image two exposures are saved separately.

The basic principle of adaptive correlation is an iterative method: From an initial guessed offset value, an offset is introduced from the first window to the second window. The resulting vector is validated and used as a new estimate for window offset. This time, a new study is performed with a smaller interrogation area. The main advantage of using the shifted window is to capture images by leaving the interrogation area between the two light pulses. The loss of these particle images is known as " in-plane dropout ", which reduces the signal strength and the number of successful vectors obtained as a result. Capturing more particle images for each vector allows the interrogation field to be refined. It provides a sufficient number of successful vectors without increasing seed density in the flow.

3.2.6. Validation & Further Analysis

The raw images captured via the charged coupled device were analyzed with Dynamic Studio software. For each case, 2 data sets were analyzed, which are containing 1000 images for each. The adaptive correlation algorithm performed with divided 32x32 and %50 overlapped subareas. After the raw image and adaptive correlation, the Universal outliner algorithm applied to interpolate and substitute spurious vectors, which were ensured at 3% and below the whole vector field during the experiment (Westerweel,2005). Matlab software used to process the instantaneous vector fields to get contours.

4. RESULTS

Since this study focuses on an improved bluff body shape, one of the most investigated geometry, i.e. a circular cylinder, was first considered as a start-up. The results of cylinder flow has been used for validating the measurements and comparison with the bio-body to elaborate the effectiveness of this novel shape on the general flow characteristics around bluff bodies. Therefore, the results of the flow around a circular cylinder will be presented first, then the evaluated results of bio-body will be compared by means of time-averaged and instantaneous flow features

4.1. Cylinder

4.1.1. Time Averaged Results

Time-averaged vorticity contours superimposed with the streamline topologies, time-averaged streamwise and transverse velocity contours are presented in Figure 4.1. Well-defined vortices are obvious with recirculation regions for all Re numbers in the near wake of the cylinder, which can be seen on the first column of Figure 4.1. The locations of focal points and saddle are indicated as F_1, $F_{2,}$ and S, respectively. Focal points in Figure 1 are symmetrically obtained with a certain distance apart from each other. Locations of saddle and focal points get closer to the cylinder base (rear stagnation point) with increasing Reynolds number, i.e. the saddle point is obtained at x/D = 1.91, x/D = 1.02, and x/D = 1.04 for Re_D = 4450, Re_D = 8900 and Re_D = 13400 respectively. This condition is an indication of narrowing the wake, in agreement with the literature (Basu,1986; Sarpkaya,2004; Zdravkovic,1997). The focal points for Re_D = 5000 are almost symmetrical at x/D =1.0, similar to the results of Ozkan et al. (2017), Gim et al. (2011) and Aljure et al. (2015).

Vortex formation length (L_f) is defined as the distance between the cylinder centroid and root mean square stream-wise velocity peaks(Rodriquez et al.,2015;Norberberg,1998;Aljure et al.;2015,Ozkan et al.,2017). The vortex formation length is obtained at x/D = 1.71 , x/D = 0.98 and x/D = 1.07 from the base of the cylinder for Re_D =4450, Re_D = 8900 and Re_D = 13400 respectively. The vortex formation length found approximately the same for Re_D = 15 x 10^3 , 13.4 x 10^3, 8.9 x 10^3, respectively. Moreover the vortex formation length at Re_D = 15 x 10^3 found in good agreement with Zdravkovich (1997) .

In the second column of figure 4.1, streamwise velocity contours for all Reynolds numbers are presented. For all cases, a negative flow region is obtained as the representative of recirculating flow in the near wake. In accordance with the decrease in vortex formation length, the location of adverse flow gets closer to the cylinder base with increasing Re_D.

The transverse velocity contours are shown in the third column of figure 4.1. The shear layers separated from the cylinder form two small-scale clusters and two large-scale clusters downstream of the cylinder; both small-scale and large-scale clusters were found further away from the rear of the cylinder as the Reynolds number decreases.

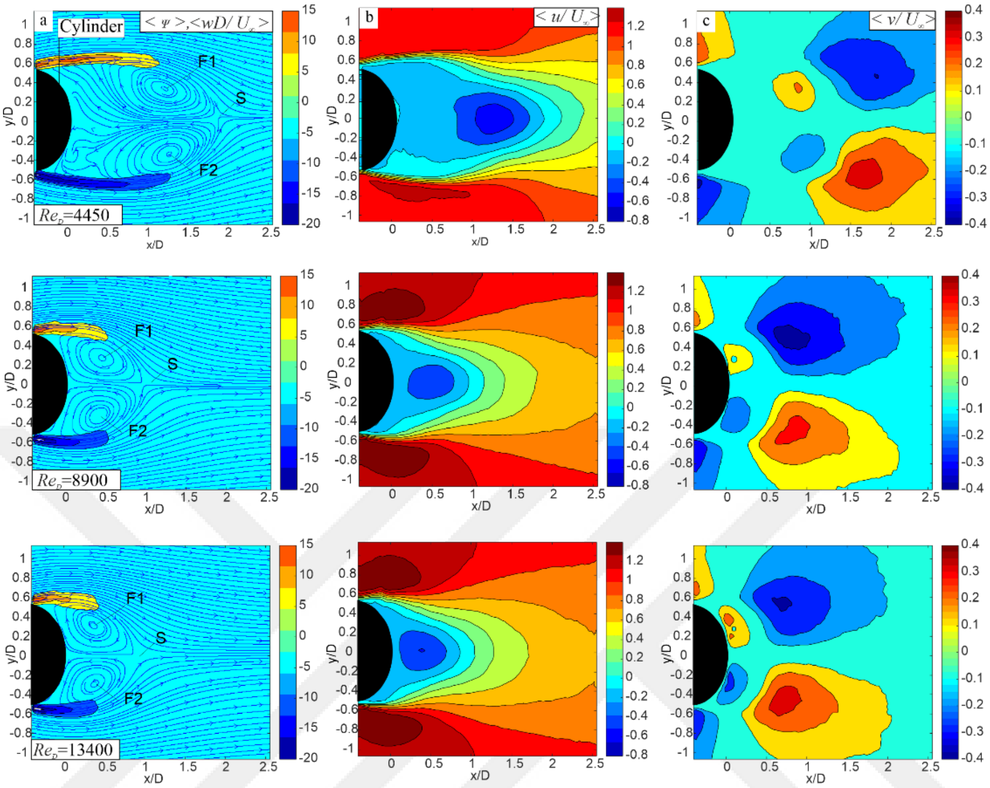

Figure 4.1. (a) Time-averaged vorticity contour superimposed on time-averaged$<wD/\ U_\infty>$streamline topology $<\ \psi\ >$(b) Time-averaged streamwise velocity contour$<\ u/\ U_\infty>$ (c) Time-averaged transverse velocity contour $<\ v/\ U_\infty>$

Distribution of Reynolds normal stresses in streamwise and transverse directions and Reynolds shear stresses are shown in figure 4.2. All of the contour's axes were scaled with respect to the diameter of the cylinder. The Reynolds normal stresses and the Reynolds shear stresses normalized with the square of freestream velocity. The distributions of streamwise Reynolds normal stress $<u'u'>/U_\infty^2$ introduce a double-peak pattern with a maximum value of $<u'u'>_{max}/U_\infty^2$ 0.24, 0.36 and 0.392 for Re_D=4450, Re_D=8900, Re_D=13400 respectively. The peak location of streamwise Reynolds stress is obtained at x/D=1.53, x/D=0.65 and x/D=0.47 for Re_D=4450, Re_D=8900, Re_D=13400 respectively. In contrast to that, due to the interaction of separated shear layers along the centerline, a single peak is obtained for $<v'v'>/U_\infty^2$. The maxima for $<v'v'>_{max}/U_\infty^2$ were found to be 0.315, 0.58 and 0.64 at *x/D*=1.77, *x/D*=1.01and *x/D*=0.95 for Re_D=4450, Re_D=8900, Re_D=13400, respectively. The distributions of the time-averaged Reynolds shear stress $<u'v'>/U_\infty^2$ pattern in the last column of Figure 4.2 is found to be almost symmetrical for all cases along the centerline of the cylinder. The location of maximum Reynolds shear stress moves backward to the rear stagnation point, which were found at *x/D*=1.92, *x/D*=0.9, and *x/D*=0.895 for Re_D=4450, Re_D=8900, Re_D=13400, respectively.

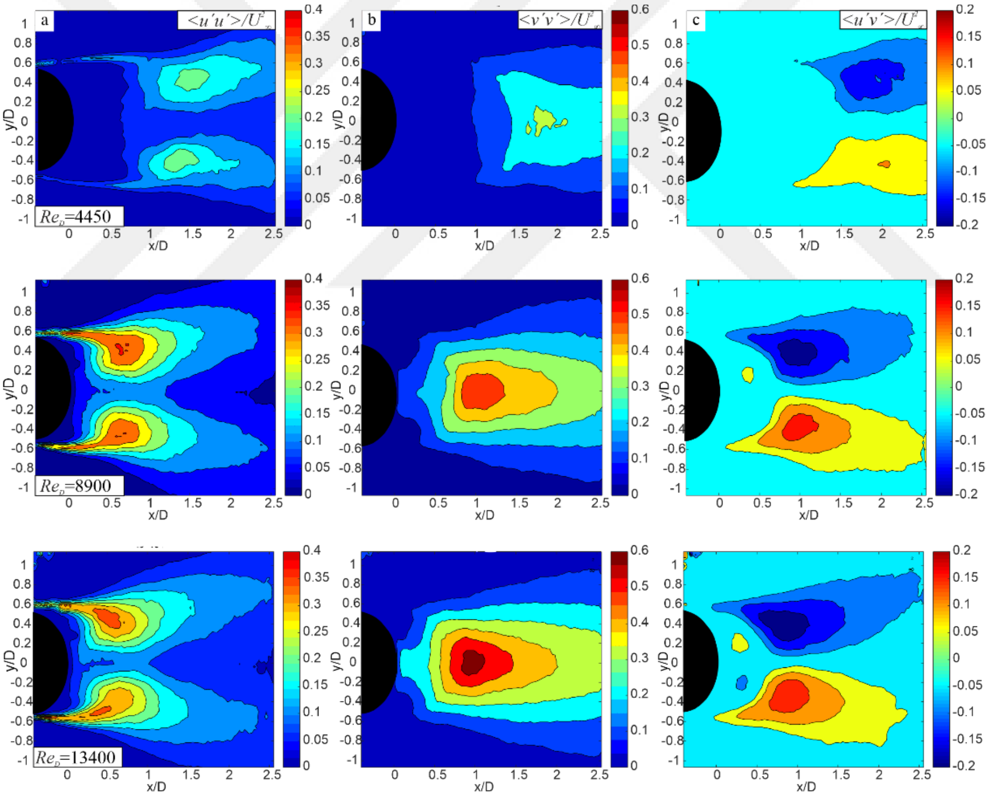

Figure 4.2. (a) streamwise Reynolds normal stresses $<u'u'>/U_\infty^2$ (b) transverse Reynolds normal stresses $<v'v'>/U_\infty^2$ (c) Reynolds shear stresses $<u'v'>/U_\infty^2$

4.1.2. Instantaneous Vortices

The contours of instantaneous vorticity for Re_D= 13400 are shown in figure 4.3. Here, the evolution of vortex shedding is presented for one cycle of the period. *T0* indicates the time at the beginning of the period, and *T1* indicates the time at the end of the period at that Reynolds number *T0+ 1/f* (*f*: frequency of vortex shedding phenomena for that Reynolds number). At $t= T0$ vortex rolling-down in the near wake from generated shear layer, six instantaneous vortex contours were shifted between each image, i.e. the time between each contour is $6\Delta t$ (Δt=1/15s). The lower vortex shed by the upper vortex until the time reach $t= T0 + 4x(6\Delta t)$. The vortex shedding period ends up with the next roll-in of the upper vortex, i.e. at $t= T0 + 3.6s$ corresponding to a frequency f=1/3.6 =0.2777. Here we found shedding frequency different from the FFT results with a 5.3% error.

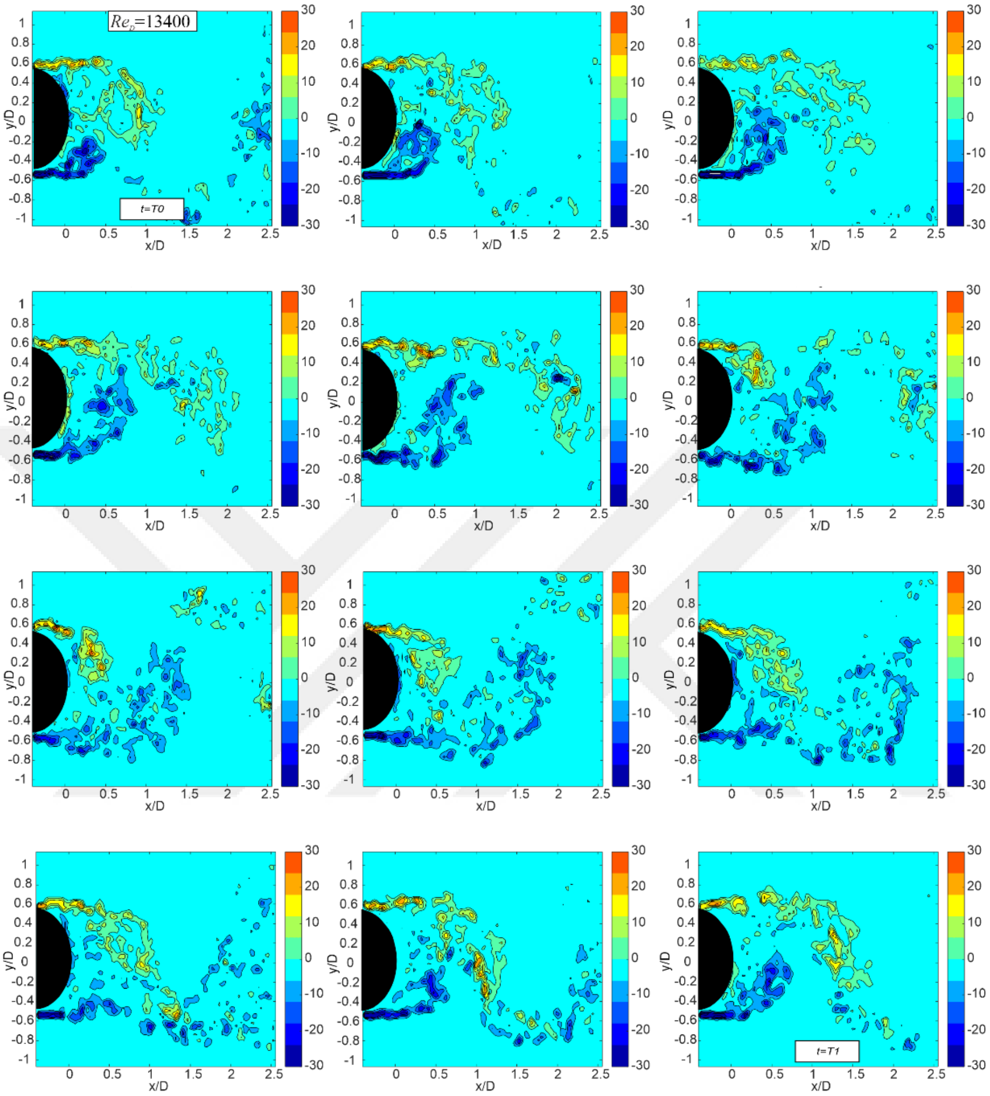

Figure 4.3. Vortex shedding phenomena for Reynolds number 13400

The shedding of vortices for Re_D= 8900 is presented in Figure 4.4. Here, the blue and red contours present the positive clockwise and negative counter-clockwise vortices, respectively. At t=$T0$, the vortex is rolling-up in the near wake from the generated shear layer, three instantaneous vortex contours were shifted between each image, i.e. the time between each contour is $3\Delta t$ (Δt=1/15s). At t= $T0$ + 4x(3Δt), the upper vortex is totally shed by the lower vortex. This effect is valid until At t= $T0$ + 5x(3Δt), where the upper vortex rolls-up into the cylinder wake. The periodic shedding of vortices ends up with the next roll-in of lower vortex, i.e. t= $T0$ + 1.8s corresponding to a frequency f=1/1.8 =0.555. Here we found shedding frequency different from the FFT results with a 6.3% error.

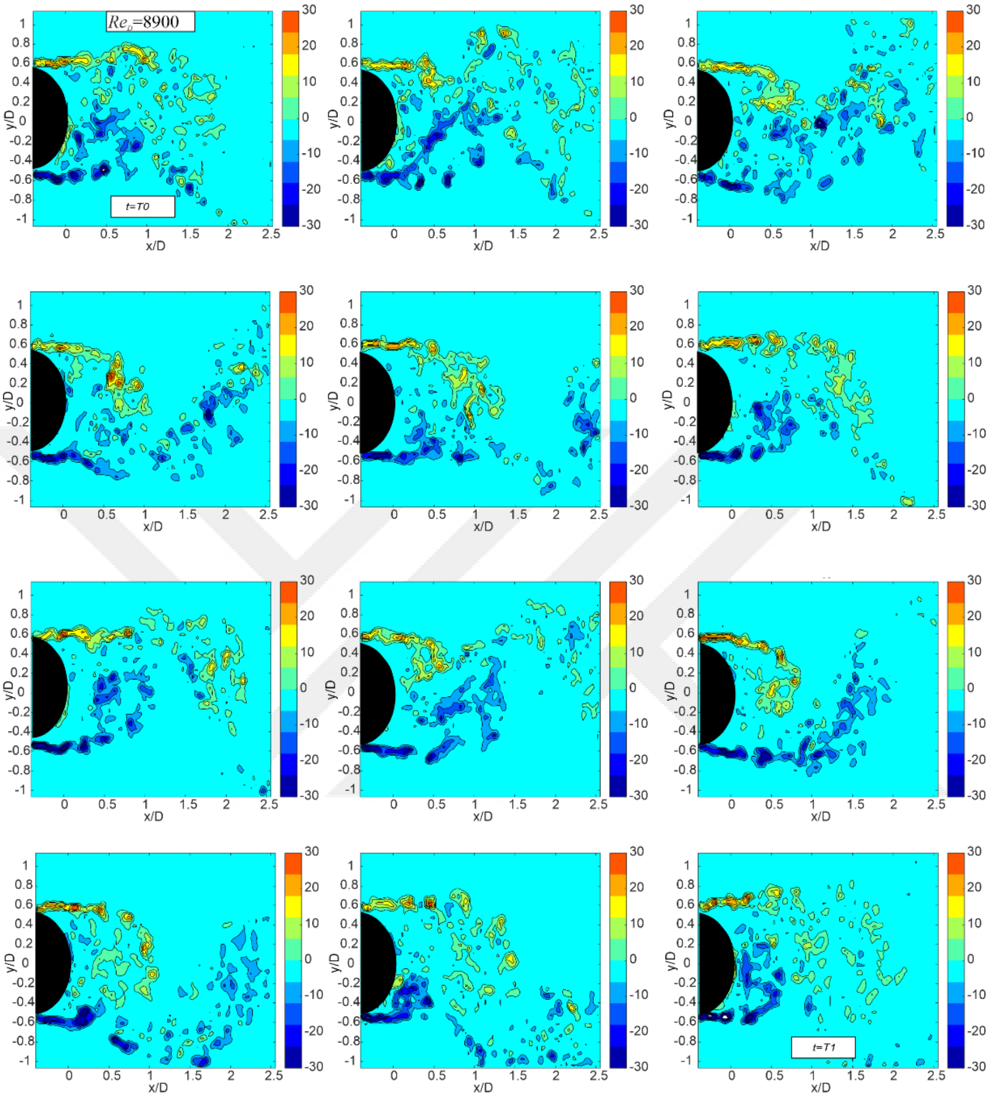

Figure 4.4. Vortex shedding phenomena for Reynolds number 8900

The shedding of vortices for Re_D= 4450 is presented in Figure 4.5. Here, the blue and red contours present the positive clockwise and negative counter-clockwise vortices, respectively. At $t=T0$, the vortex is rolling-up in the near wake, two instantaneous vortex contours were shifted between each image, i.e. the time between each contour is $2\Delta t$ (Δt=1/15s). At $t= T0 + 4x(2\Delta t)$, the upper vortex is totally shed by the lower vortex. This effect is valid until At $t= T0 + 8x(2\Delta t)$, where the upper vortex rolls-up into the cylinder wake. The periodic shedding of vortices ends up with next roll-in of lower vortex, i.e. $t= T0$ + 1.333s corresponding to a frequency f=1/1.333 =0.75. Here we found shedding frequency different from the FFT results with a 2.6% error.

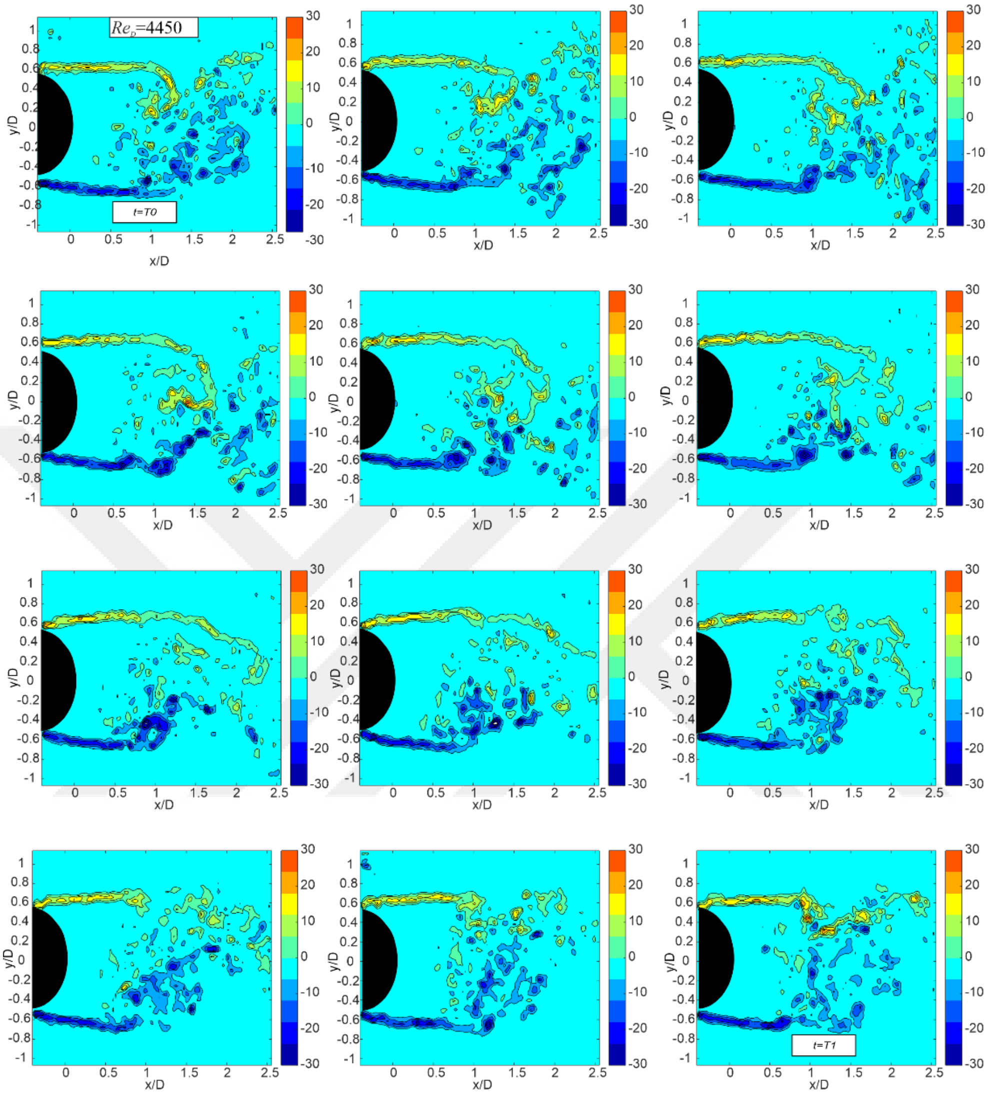

Figure 4.5. Vortex shedding phenomena for Reynolds number 4450

4.1.3. Spectral Analysis

Figure 4.6 shows the power spectral analysis for the cylinder. The power spectrum analysis was performed based on the Fast Fourier transform (FFT), which provides the vortex shedding frequency of obtained data (Ozkan et al., 2017). In order to compare various cases, the Strouhal number is also calculated and presented to get information about the periodic flow motion of a body.

In flows characterized by a periodic motion, the Strouhal number is correlated with the oscillations of the flow and expressed by the following equation:

$$St = \frac{fD}{U_\infty} \tag{4.1}$$

Here f is the vortex shedding frequency, D is the diameter of the cylinder and U_∞ Is the free-stream velocity. At high Strouhal number, the flow dominated by oscillations, but at low Strouhal number, the oscillations swept via moving fluid (Katopodes,2019).

According to results presented in Figure 4.6, the vortex shedding frequency is obtained as f=0.77, 0.52, 0.263 corresponding to Strouhal numbers of St=0.22, 0.2, 0.22 for Re_D=4450 , Re_D=8900 and Re_D=13400 respectively.

All results closely agree with the results of Roshko(1953) and White(1979), according to Fig. 4.7. The locations to measure power spectral analysis were taken away from the cylinder in agreement with Ozkan, Firat, and Akilli (2017).

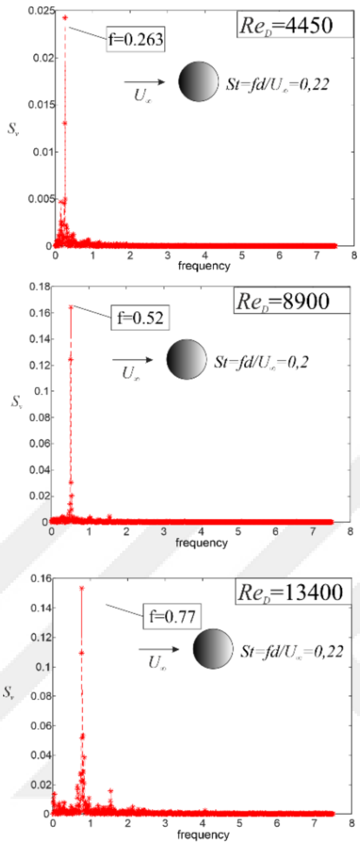

Figure 4.6. Power spectral analysis at x/D=1.6 and y/D=1.1

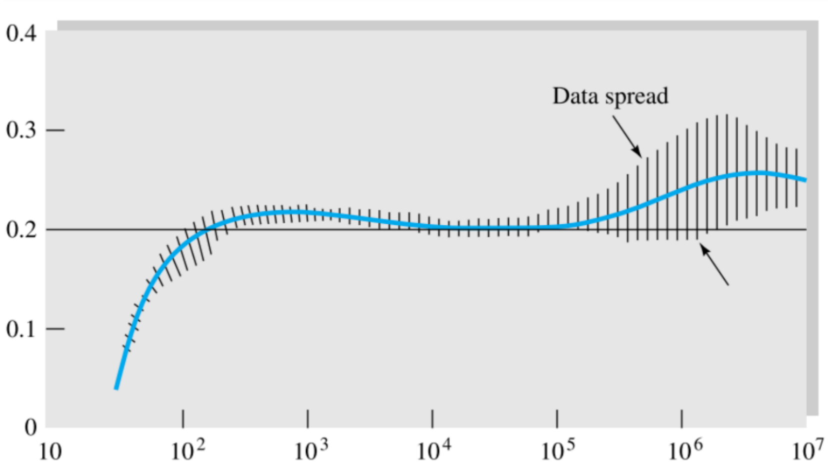

Figure 4.7. Reynolds number versus the Strouhal number (White, 1979).

4.2. Bio-Body

Since the flow around the novel bio-body is highly three-dimensional, various planes and sections were considered for PIV measurements. In this section, the results of the bio-body are presented step by step for those planes and sections.

4.2.1. Planview

4.2.1.1. Midplane Section

Two fields of view were considered for the bio-body to fully elaborate the flow structure around the body, together with near and far wakes. Both of them are presented in succession for the mid plane section. Time-averaged vorticity contours superimposed with the streamline topologies, streamwise and transverse velocity contours are presented in Figures 4.8 and 4.9. For all Re numbers, All of the axes were normalized with the bio body's hydraulic diameter, D_h. For the same contour type of different Reynolds numbers, same contour level ranges, increments of contours, color bar ranges were taken to compare different Reynolds numbers.

It can be seen by the streamline topology that streamlines are pivoting around the two focal points indicated by F1 and F2. These two recirculating zones get closer, and fluid gains zero velocity at a point called the saddle point designated by S (Rodríguez et al., 2015). The saddle point is obtained at $x/D_h = 0.95$, $x/D_h = 0.85$and $x/D_h = 0.75$ for $Re_D = 8900$, $Re_D = 13400$ and $Re_D = 17500$, respectively. In the same way with cylinder results, these results appeared in corroborate way that the distance of wake region and the Reynolds number inversely proportional.

In the second column of figure 4.8, streamwise velocity contours for all Reynolds numbers are presented. A negative flow region was obtained for all cases, which indicates recirculating flow in the near wake. In accordance with the decrease in vortex formation length, the location of adverse flow gets closer to the rear stagnation point of the bio-body with increasing Re_D.

The transverse velocity contours are shown in the third column of Figure 4.8. In contrast to cylinder results, the shear layers separated from the bio-body only form two large-scale clusters in downstream; The large-scale clusters behind the bio-body are found at a larger distance as the Reynolds number decreases.

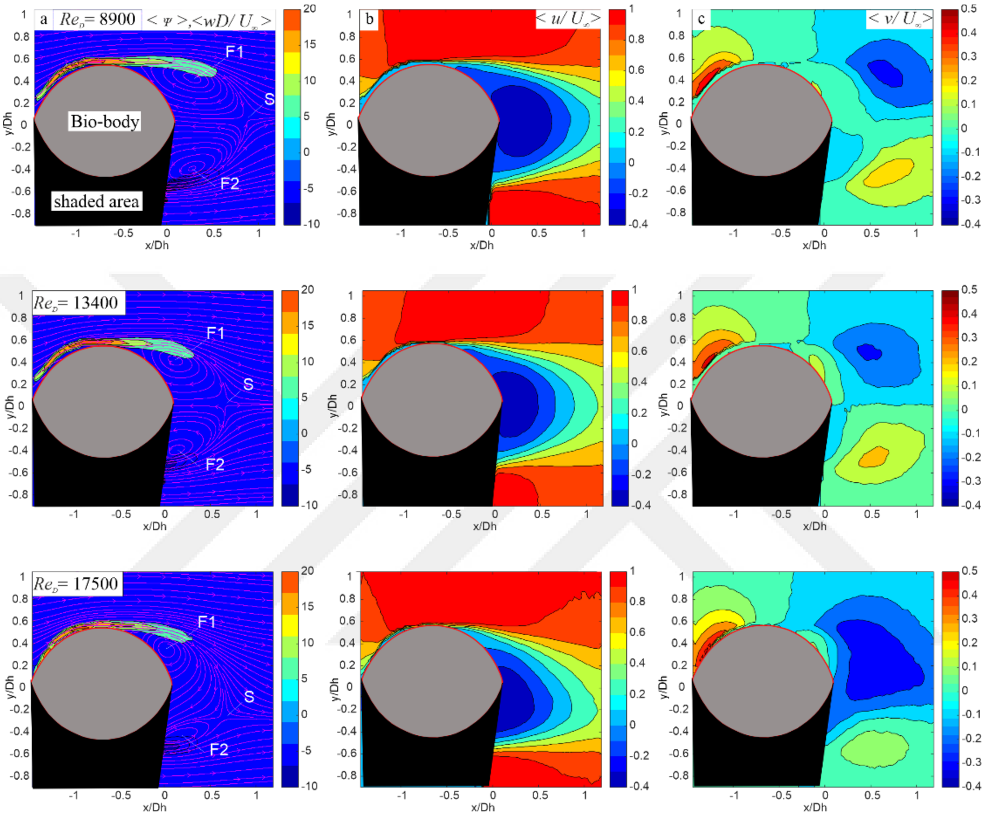

Figure 4.8. (a) Time-averaged vorticity contours superimposed with $<wD/ U_\infty>$ streamline streamline topology$< \Psi >$ (b) streamwise velocity contour$< u/ U_\infty>$ (c) transverse velocity contour $< v/ U_\infty>$

The far wake of the body presented in Fig. 4.9. Here, the vortices are almost symmetrical with two well-defined focal points (F1 and F2). The maximum value of streamwise velocity is observed on both sides of the bio-body. The saddle point is obtained at x/ D_h =0.88, x/ D_h = 0.81, and x/D_h = 0.72 for Re_D = 8900, Re_D = 13400 and Re_D = 17500, respectively. Which indicates the decrease in vortex formation length by increasing Re_D. These results point out that narrowing the wake region with Re_D is in agreement with cylinder results.

For all cases, the negative flow region describes the recirculating flow behind the bio-body that is getting further away from the rear of the bio-body as the Reynolds number decreases.

In the third column of figure 4.9, transverse velocity contours are shown. Differently from the cylinder transverse velocity pattern, the separated shear layers form two dominant large-scale clusters downstream of the bio-body. This might be an indication of the non-interacting vortices in the near wake of bio-body.

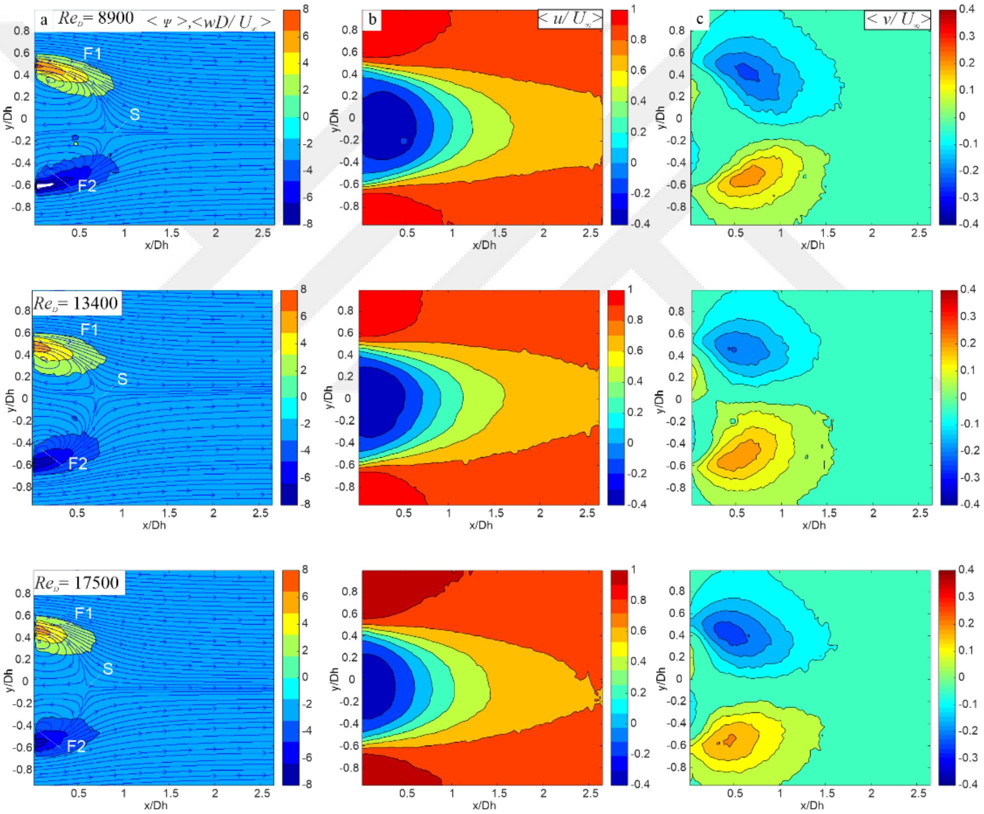

Figure 4.9. (a) Time-averaged vorticity contours superimposed with $<wD/ U_\infty>$ streamline topology $< \Psi >$ (b) streamwise velocity contour $< u/ U_\infty>$ (c) transverse velocity contour $< v/ U_\infty>$

Figure 4.10 and 4.11 show the distributions of streamwise and transverse Reynolds normal stresses and Reynolds shear stress. Both Reynolds normal and Reynolds shear stresses were normalized with the square of free stream velocity. The axes were scaled with respect to the hydraulic diameter of the bio-body. The distribution of streamwise Reynolds normal stress $<u'u'>/U_\infty^2$ introduce a double-peak pattern with a maximum value of 0.12, 0.17 and 0.17 for Re_D=8900, Re_D=13400, Re_D=17500 respectively. The peak location of streamwise Reynolds stress is obtained at x/D_h =0.57, x/D_h =0.195 and x/D_h =0.25 for Re_D=8900, Re_D=13400, Re_D=17500 respectively. In contrast to that, due to the interaction of separated shear layers along the centerline, a single peak is obtained for $<v'v'>/U_\infty^2$. The value of $<v'v'>_{max}/U_\infty^2$ are evaluated to be 0.088, 0.102 and 0.086 for Re_D=8900, Re_D=13400, Re_D=17500, respectively. Besides, the locations of peak values for $<v'v'>_{max}/U_\infty^2$ were obtained at x/D_h =0.9, x/D_h =0.62.and x/D_h =0.86 for Re_D=8900, Re_D=13400, Re_D=17500 respectively. The distribution of the time-averaged Reynolds shear stress $<u'v'>_{max}/U_\infty^2$ pattern was found to be asymmetric along the centerline of the bio-body. In figure 4.10, the peak value of Reynolds shear stress was found at x/D_h =0.73, x/D_h =0.33, and x/D_h =0.41 for Re_D=8900, Re_D=13400, Re_D=17500, respectively.

The Reynolds shear stress patterns of the bio-body differ from those of the cylinder. Bio-body consists of only two large-scale clusters in downstream. Well-defined Reynolds shear stress patterns indicate 33.5% and 30.9% lower Reynold stress in magnitude compared to the cylinder for Re_D= 8900 and Re_D= 13400, respectively.

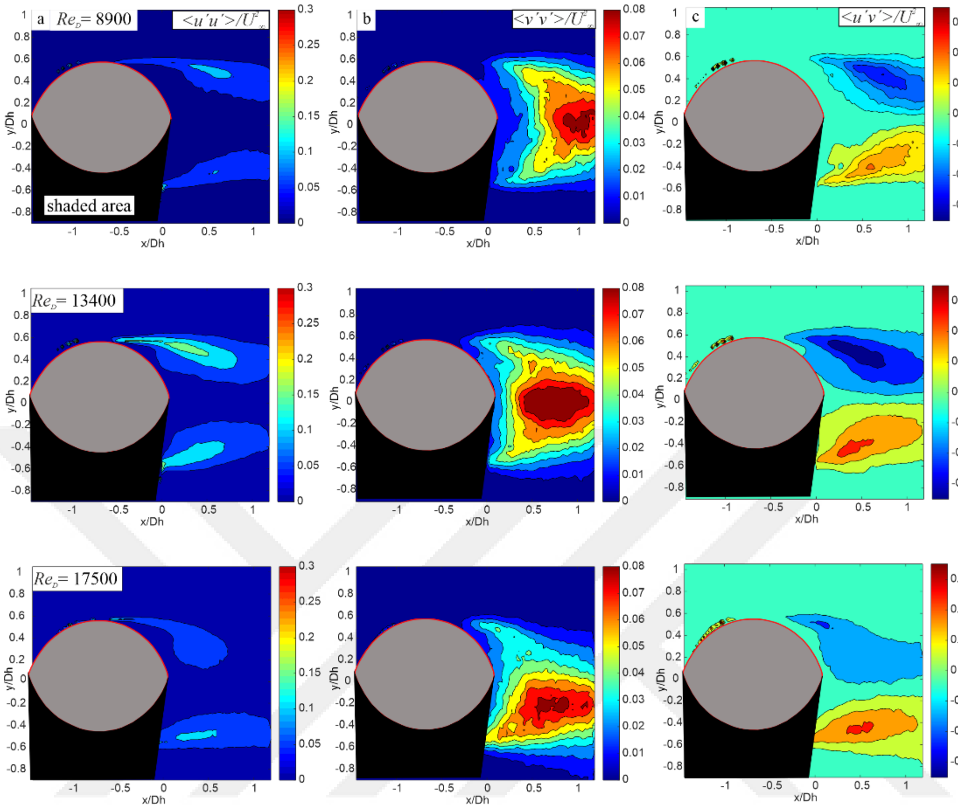

Figure 4.10. streamwise Reynolds normal stress$<u'u'>/U^2_\infty$ (b) transverse Reynolds normal stress$<v'v'>/U^2_\infty$ (c) Reynolds shear stress$<u'v'>/U^2_\infty$

In Figure 4.11, the distributions of streamwise Reynolds normal stress $<u'u'>/U^2_\infty$ appear including a double-peak pattern with a maxima of 0.16, 0.155 and 0.164 for Re_D=8900, Re_D=13400, Re_D=17500 respectively. The peak location of streamwise Reynolds stress is obtained at x/D_h =0.43, x/D_h =0.27 and x/D_h =0.32 for Re_D=8900, Re_D=13400, Re_D=17500, respectively. On the other hand, the interaction of separated shear layers along the centerline led to the single peaks of $<v'v'>/U^2_\infty$. The magnitude of $<v'v'>_{max}/U^2_\infty$ is evaluated to be 0.11 for all cases. Besides, the locations of peak values for $<v'v'>_{max}/U^2_\infty$ were obtained at x/D_h =0.91, x/D_h =0.88.and x/D_h =0.53 for Re_D=8900, Re_D=13400, Re_D=17500 respectively. The Reynolds shear stress patterns in the last column demonstrate two large clusters along the centerline which vary in magnitude for all Re_D.

In figure 4.11, the peak value of Reynolds shear stress was obtained at $x/D_h=0.8$, $x/D_h=0.35$ and $x/D_h=0.374$ for Re_D=8900, Re_D=13400, Re_D=17500 respectively. Reductions in in $\langle u'v'\rangle_{max}/U_\infty^2$ of 71.6% and 70.2% were obtained for Re_D =8900, Re_D =13400 respectively, compared to the cylinder.

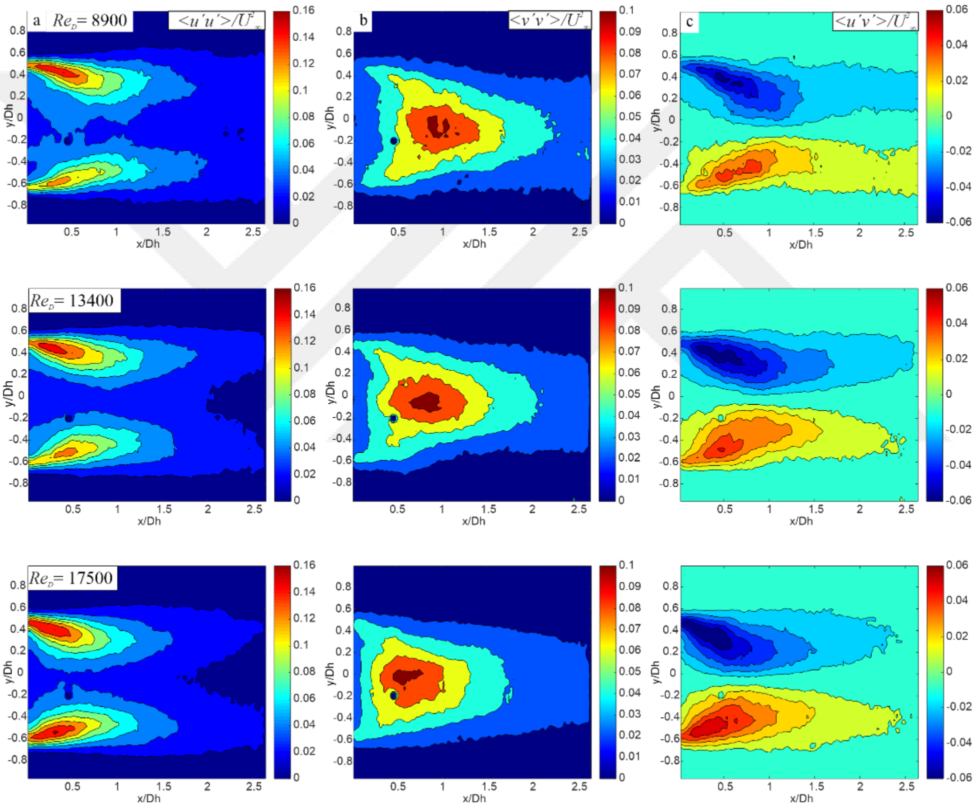

Figure 4.11. streamwise Reynolds normal stresses $\langle u'u'\rangle/U_\infty^2$ (b) transverse Reynolds normal stresses $\langle v'v'\rangle/U_\infty^2$ (c) Reynolds shear stresses $\langle u'v'\rangle/U_\infty^2$

4.2.1.2. Quarter Plane Section

The measurements obtained at H/2 are presented in this section to reveal the flow structure far from the body’s centerline. Time-averaged vorticity contours superimposed with the streamline topologies, time-averaged streamwise and transverse velocity contours are presented in figures 4.12 and 4.13. Contour levels and increments were specified to be identical for varying Re_D for better comparison. It is observed in Figure 4.12 that the vortices indicated by two main focal points, namely F1 and F2, occupies a region up to the saddle point (S) downstream of the bio-body. The obtained vortices are almost symmetrical along the body centerline; however, little asymmetry is the case for Re_D=13400 due to the inaccuracy in the measurement setup. The evaluated saddle points were obtained at $x/D_h = 0.96$, $x/D_h = 0.87$, $x/D_h = 0.75$ for Re_D=8900, Re_D=13400, Re_D=17500, respectively. It should be noted that the results indicate narrowing of the wake region with Reynolds number, similar with cylinder flow. Moreover, the vortices formed from the upper and lower shoulder of the bio-body tend to move into the wake, as an indication of the interaction of the vortices, hence the occurrence of vortex shedding. In the second column of Figure 4.12, streamwise velocity contours for all Reynolds numbers are presented. A negative flow region was obtained for all cases, which indicates recirculating flow in the near wake. In accordance with the decrease in vortex formation length, the location of adverse flow gets closer to the bio-body base with increasing Re_D. Finally, the transverse velocity contours are shown in the third column of figure 4.12. The results present identical flow structures with that of the circular cylinder, i.e. the separated shear layers form two large clusters and two small clusters downstream of the bio-body. The large-scale clusters behind the bio-body are shifted in downstream as the Re_D increases.

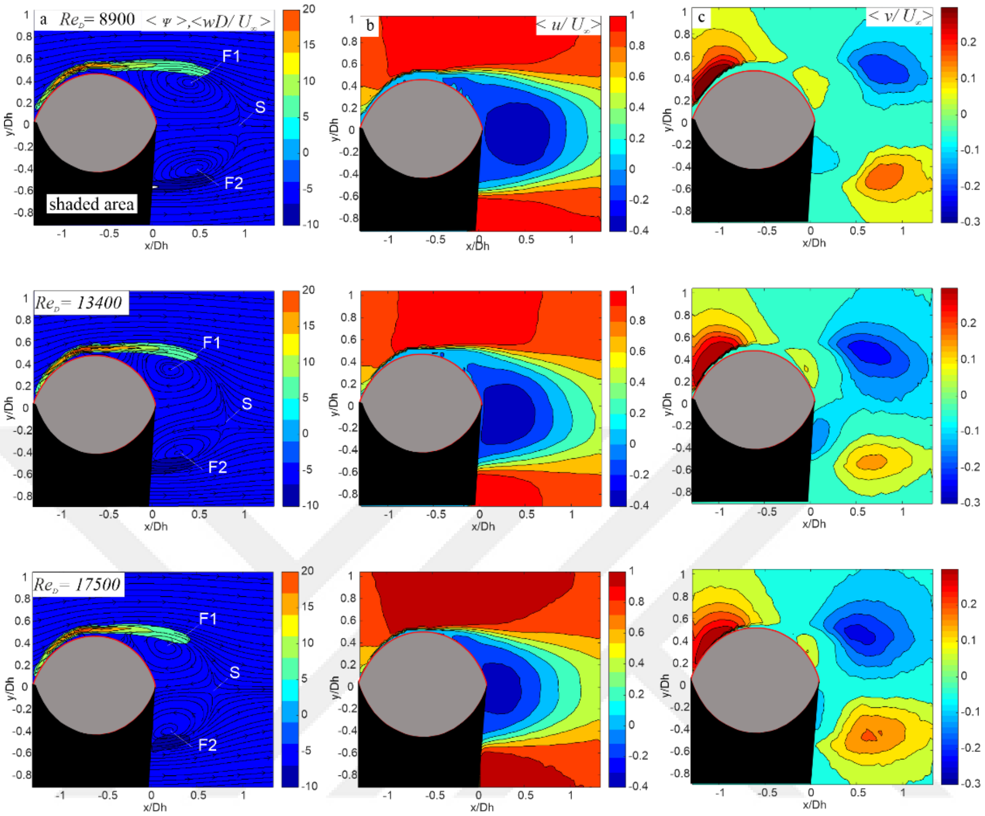

Figure 4.12. (a) Time-averaged vorticity contours superimposed with $<wD/ U_\infty>$ streamline topology $< \psi >$ (b) streamwise velocity contour $< u/ U_\infty>$ (c) transverse velocity contour $< v/ U_\infty>$

Figure 4.13 presents the streamwise, and transverse Reynolds normal stresses, together with Reynolds shear stresses for all Re_D. The distribution of streamwise Reynolds normal stress $<u'u'>/U_\infty^2$ introduce a double-peak pattern with maximum values of 0.25, 0.25, and 0.29 for Re_D=8900, Re_D=13400, and Re_D=17500 respectively. The peak location of streamwise Reynolds stress is obtained at x/ D_h =-0.84, x/ D_h =-0.81 and x/ D_h =-0.81 for Re_D=8900, Re_D=13400, Re_D=17500, respectively. In contrast to that, due to the interaction of separated shear layers along the centerline, a single peak is obtained for $<v'v'>/U_\infty^2$. The values of $<v'v'>_{max}/U_\infty^2$ are evaluated to be 0.067, 0.072 and 0.065 for Re_D=8900, Re_D=13400, Re_D=17500, respectively. Besides, the locations of peak values for

$<v'v'>_{max}/U_\infty^2$ were obtained at x/D_h =1.01, x/D_h =0.98 and x/D_h =0.85 for Re_D=8900, Re_D=13400, Re_D=17500 respectively.

The distributions of the time-averaged Reynolds shear stress $<u'v'>_{\max}/U_\infty^2$ in the third column of Fıgure 4.13 are found to be asymmetric along the centerline of the bio-body. The peak values of Reynolds shear stress were obtained at x/D_h =0.53, x/D_h =0.61, and x/D_h =0.37 for Re_D=8900, Re_D=13400, Re_D=17500, respectively. It should be noted that the Reynolds shear stress pattern for bio-body consists of only two large-scale clusters downstream of the bio-body, compared with the cylinder results (see Figure 4.2). The maximum values of Reynolds shear stress were evaluated to be 69.8% and 72.2% less compared to the cylinder for Re_D= 8900 and Re_D= 13400 cases, respectively. According to the lower fluctuations in the wake, it can be concluded that the bio-body might possess better aero-hydrodynamic characteristics than that of a circular cylinder.

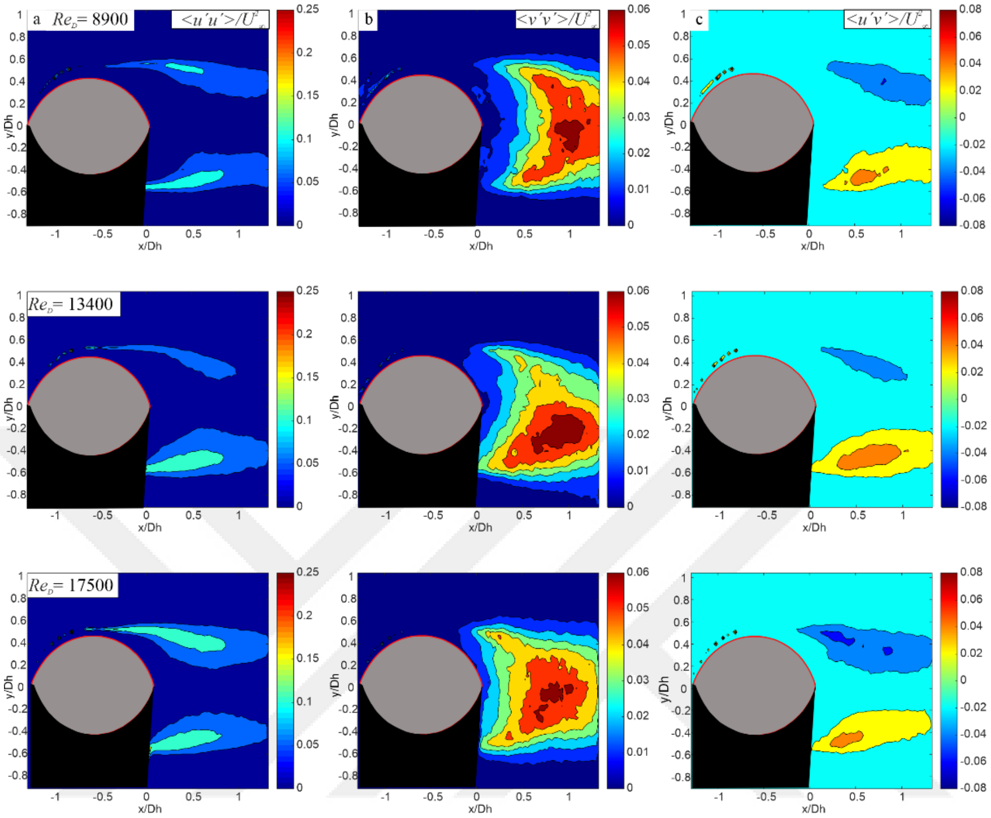

Figure 4.13. (a) streamwise Reynolds normal stresses $<u'u'>/U_\infty^2$(b) transverse Reynolds normal stresses$<v'v'>/U_\infty^2$ (c) Reynolds shear stresses$<u'v'>/U_\infty^2$

4.2.2. Sideview

4.2.2.1. Midplane Section

Time-averaged vorticity contours superimposed with the streamline topologies, time-averaged streamwise and transverse velocity contours are presented in figure 4.15. Contour levels and increments were specified to be identical for varying Re_D for better comparison.

It is observed in Figure 4.15 that the vortices indicated by two main focal points, namely F1 and F2, reaches up to the saddle point (S) downstream of the bio-body. The vortices were found to be asymmetric for all cases. The evaluated saddle points were obtained at $x/D_h = 0.88$, $x/D_h = 0.72$, $x/D_h = 0.56$ for Re_D=8900, Re_D=13400, Re_D=17500, respectively. These results indicate narrowing of the wake region with Reynolds number, similar to the cylinder flow. The vortices formed from the upper and lower shoulder shed alternately, generating a low-pressure region downstream of the body. Moreover, these vortices tend to move into the wake as a sign of interaction of the vortices, hence the vortex shedding.

In the second column of Figure 4.15, streamwise velocity contours for all Reynolds numbers are presented. A negative flow region was obtained for all cases as an indication of the recirculation region downstream of the bio-body. In conformity with the decrease in vortex formation length, the end of the adverse flow region gets closer to the bio-body base with increasing Re_D. Finally, the transverse velocity contours are shown in the third column of figure 4.15, in which the results introduce an indistinguishable distribution with that of the circular cylinder, i.e. the separated shear layers form two large clusters and two small clusters downstream of the bio-body. The large-scale clusters behind the bio-body are shifted in downstream as the Re_D decreases.

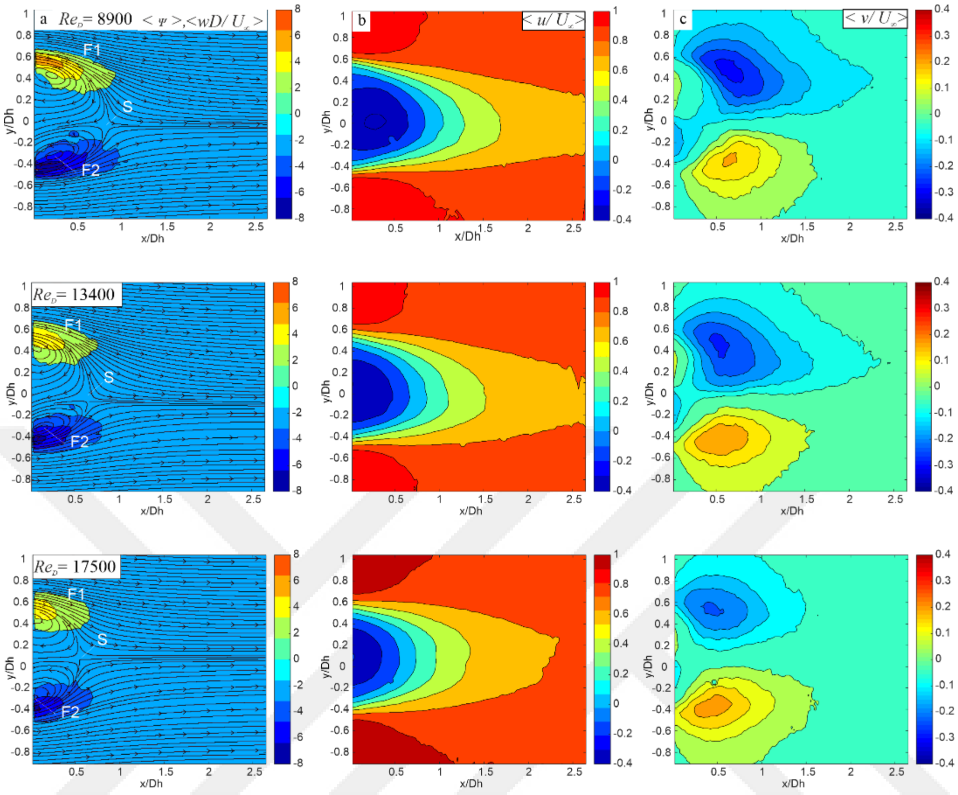

Figure 4.14. (a) Time-averaged vorticity contour $<wD/\ U_\infty>$ superimposed on time-averaged streamline topology $<\ \psi\ >$ (b) Time-averaged streamwise velocity contour $<u/\ U_\infty>$ (c) Time-averaged transverse velocity contour $<v/\ U_\infty>$

Figure 4.16 presents the time-averaged streamwise and transverse Reynolds normal stresses, together with Reynolds shear stresses for all cases. The Reynolds normal stresses associated with the random fluctuations in streamwise direction $<u'u'>/U_\infty^2$ demonstrate a double-peak pattern with maximum values of 0.104, 0.12, and 0.163 for Re_D=8900, Re_D=13400, and Re_D=17500 respectively. The peak value of streamwise Reynolds stress is obtained at $x/\ D_h$ =0.37, $x/\ D_h$ =0.16 and $x/\ D_h$ =0.11 for Re_D=8900, Re_D=13400, Re_D=17500, respectively. However a single peak was obtained for Reynolds normal stresses in transverse direction. It can be observed in the second column of Fig.4.16that the peak magnitudes of $<v'v'>/U_\infty^2$ are found as 0.067, 0.095 and 0.13 for Re_D=8900, Re_D=13400, Re_D=17500, respectively. In addition, the locations of peak values for $<v'v'>_{max}/U_\infty^2$ were obtained at x/D_h =0.99, x/D_h =0.94 and x/D_h =0.67 for Re_D=8900, Re_D=13400, Re_D=17500 respectively.

The distributions of the time-averaged Reynolds shear stress $<u'v'>/U_\infty^2$ in the third column of Fıgure 4.16 are found to be asymmetric along the centerline of the bio-body. The extreme values of Reynolds shear stress were obtained at x/D_h =0.67, x/D_h =0.4, and x/D_h =0.27 for Re_D=8900, Re_D=13400, Re_D=17500, respectively. Unlike cylinder results, the Reynolds shear stress pattern of the bio-body consists of only two large-scale clusters downstream of the bio-body (see Figure 4.2). The extreme values of Reynolds shear stress found to be 77% and 75.4% lower in magnitude compared to the cylinder for Re_D= 8900 and Re_D= 13400 cases, respectively. The lower fluctuations in the wake indicates eligibility of the bio-body in terms of its aero-hydrodynamic efficiency over the circular cylinder.

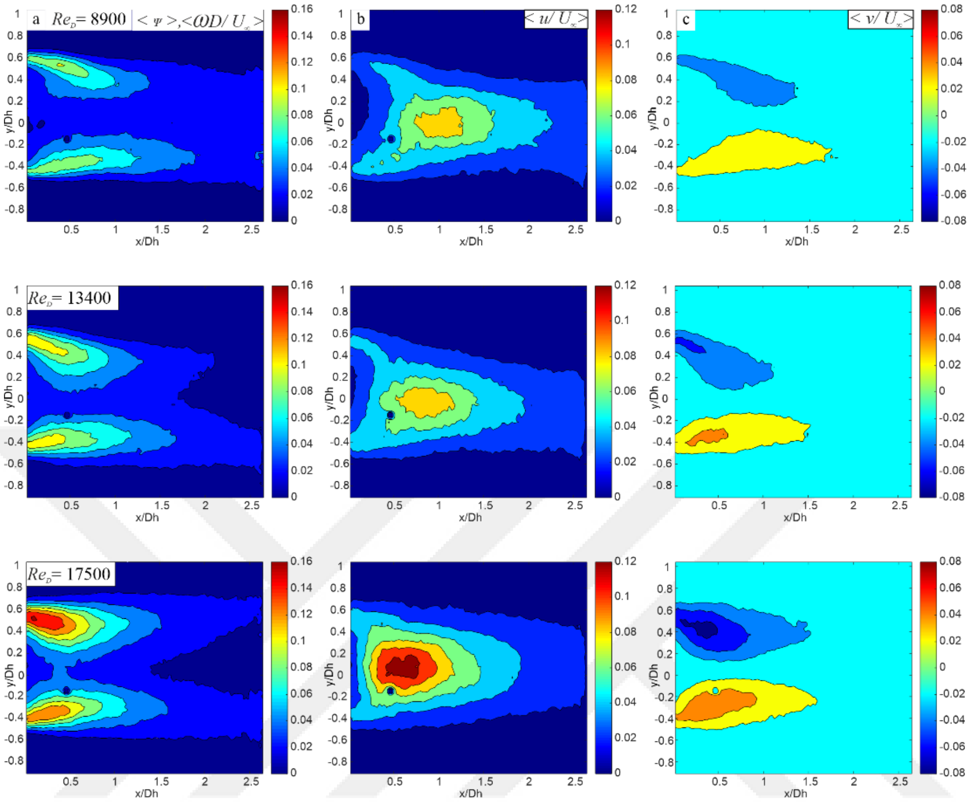

Figure 4.15. (a) streamwise Reynolds normal stresses $<u'u'>/U_\infty^2$(b) transverse Reynolds normal stresses$<v'v'>/U_\infty^2$ (c) Reynolds shear stresses$<u'v'>/U_\infty^2$

4.2.2.2. Quarter Plane Section

Time-averaged vorticity contours superimposed with the streamline topologies, time-averaged streamwise and transverse velocity contours are presented in figures 4.17 and 4.18 for all cases at L/2. Contour levels and increments were specified to be identical for varying Re_D for better comparison.

Firstly, the separated shear layers that split from the shoulder of the bio-body are in tendency to swirl around focal points, where the focal points are designated by F1 and F2. The swirling separated shear layer reaches a point where the velocity of the fluid is zero, namely the saddle point (S). The evaluated vortices were found to be almost symmetric along the centerline for all cases. The evaluated saddle points were obtained at x/ D_h = 0.82, x/ D_h = 0.67, x/ D_h = 0.66 for Re_D=8900, Re_D=13400, Re_D=17500, respectively. The wake region becomes narrower as the Reynolds number increases. Moreover, the two opposite-side vortices shed alternatively and spill over to the wake region, which yields a relatively low-pressure region as an indication of the interaction of these vortices. In the second column of Figure 4.17, streamwise velocity contours for all Reynolds numbers are presented. The streamwise velocity distribution introduces the reverse flow region, which indicates the recirculation region close to the wake of the bio-body. The reverse flow region reveals in the same way with shortening of vortex formation length with increasing Reynolds number. Finally, the transverse velocity contours are shown in the third column of figure 4.17. The dispersion of transverse velocity contours reveals two types of cluster vortical structures similar to cylinder results (see Figure 4.1).

The large-scale clusters behind the bio-body are shifted in downstream as the Re_D decreases.

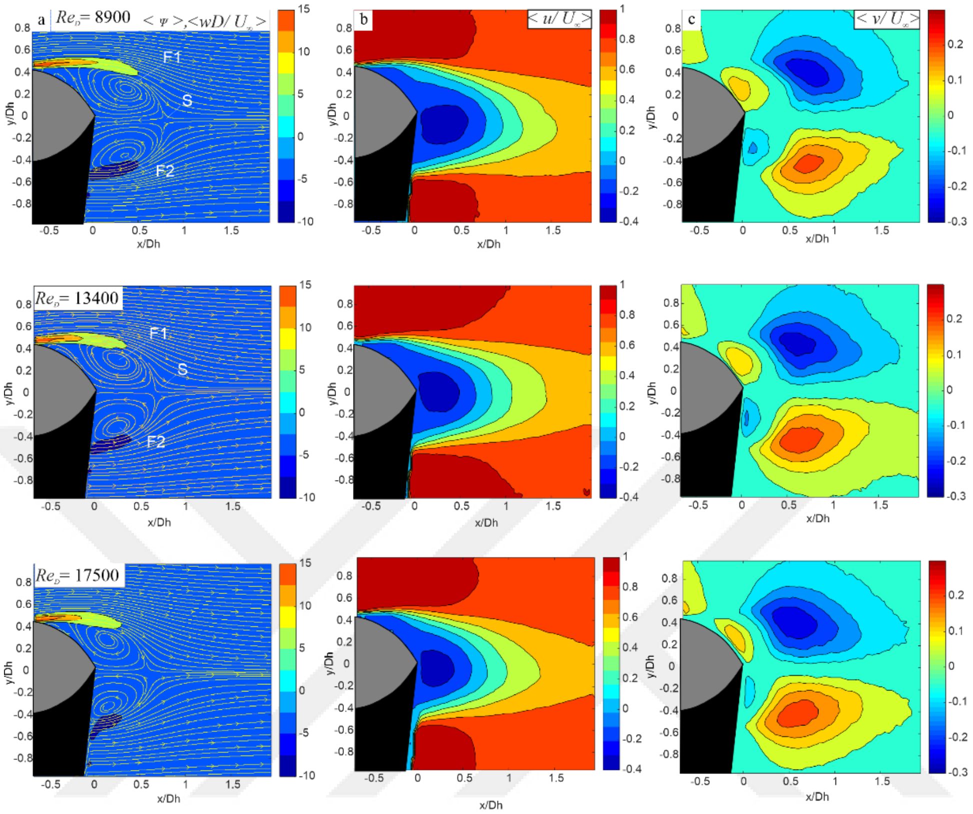

Figure 4.16. (a) Time-averaged vorticity contour $<wD/ U_\infty>$ superimposed on time-averaged streamline topology $< \Psi >$ (b) Time-averaged streamwise velocity contour $< u/ U_\infty>$ (c) Time-averaged transverse velocity contour $< v/ U_\infty>$

The evaluated saddle points were obtained at x/D = 0.82, x/D = 0.67, x/D = 0.66 for Re_D=8900, Re_D=13400, Re_D=17500, respectively.

The wake region becomes narrower as the Reynolds number increases. In the second column of Figure 4.18, streamwise velocity contours for all Reynolds numbers are presented. A negative flow region found as an indication of the recirculation region at base of the bio-body. The recirculation region is getting closer to the base of the bio-body with an increment of the Reynolds number. The transverse velocity contours are shown in the third column of figure 4.18. Unlike the cylinder results, the dispersion of transverse velocity contours reveals only two large-scale clusters; this may happen due to the lack of the measurement area to detect small clusters. The large-scale clusters getting closer to base of the bio-body in downstream as the Re_D increases.

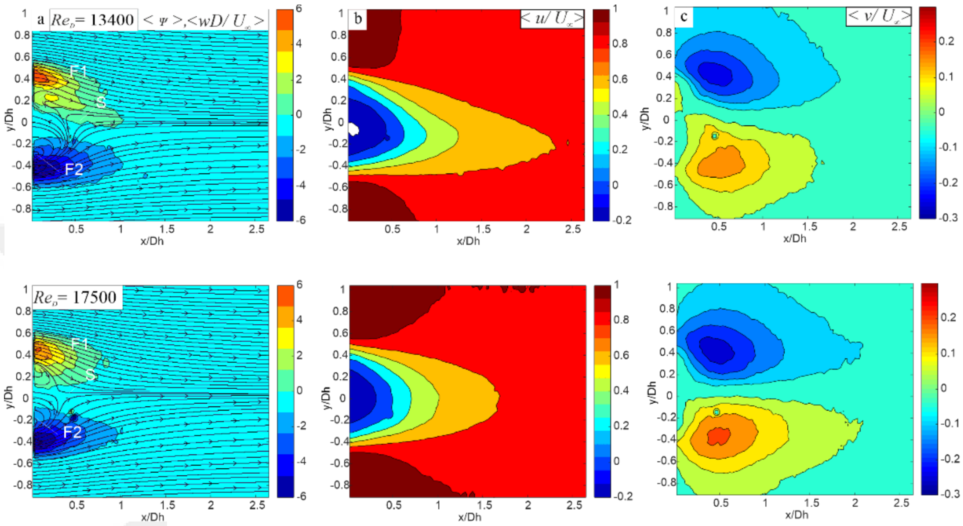

Figure 4.17. (a) Time-averaged vorticity contour $<wD/U_\infty>$ superimposed on time-averaged streamline topology $<\psi>$ (b) Time-averaged streamwise velocity contour $<u/U_\infty>$ (c) Time-averaged transverse velocity contour $<v/U_\infty>$

Figure 4.19 and 4.20 present the distributions of streamwise and transverse Reynolds normal stresses and Reynolds shear stresses. The double peak of streamwise Reynolds normal stress associated with fluctuation component of streamwise velocity $<u'u'>/U_\infty^2$ has extreme values of 0.143, 0.18 and 0.25 for Re_D=8900, Re_D=13400, Re_D=17500 respectively. Besides, The peak locations of streamwise Reynolds stress are obtained at x/D_h =0.54, x/D_h =-0.31 and x/D_h =0.001 for Re_D=8900, Re_D=13400, Re_D=17500 respectively. A single peak centered Reynold normal stress associated with fluacuating component of transverse velocity component $<v'v'>/U_\infty^2$ has extreme values of 0.067, 0.06 and 0.06 for Re_D=8900, Re_D=13400, Re_D=17500, respectively. Besides, the locations of peak values for $<v'v'>_{max}/U_\infty^2$ are obtained at x/D_h =0.83, x/D_h =0.8 and x/D_h =0.74 for

Re_D=8900, Re_D=13400, Re_D=17500 respectively. The distribution of the time-averaged Reynolds shear stress <u′v′>/U_∞^2 pattern was found to be asymmetric along the centerline of the bio-body. The Reynolds shear stress patterns of the bio-body differ from those of the cylinder. Bio-body consists of only two large-scale clusters in downstream. Well-defined Reynolds shear stress patterns indicate 68% and 80% lower values of Reynold stress compared to the cylinder for Re_D= 8900 and Re_D= 13400, respectively.

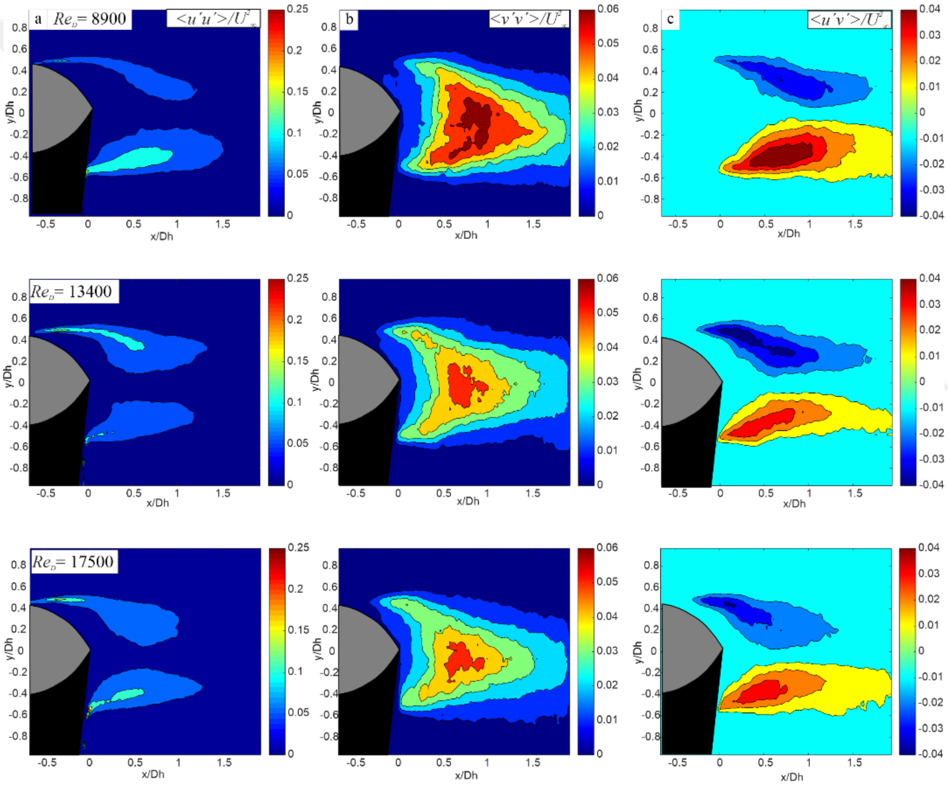

Figure 4.18. (a) streamwise Reynolds normal stresses $<u'u'>/U_\infty^2$(b) transverse Reynolds normal stresses$<v'v'>/U_\infty^2$ (c) Reynolds shear stresses$<u'v'>/U_\infty^2$

In Fig. 4.20, the distribution of Reynolds normal stresses in streamwise direction $<u'u'>/U_\infty^2$ reveal double peak with maximum value of 0.15 and 0.11 for Re_D=13400, Re_D=17500, respectively. The outlier values found at x/D_h =0.24, and x/D_h =0.27 for Re_D=13400, Re_D=17500 , respectively.

The Reynolds normal stresses associated with the fluctuation component of transverse velocity $<v'v'>/U_\infty^2$ reveal single-centre peak distribution due to the interaction of separated shear layers along the centerline. The peak values of $<v'v'>_{max}/U_\infty^2$ found as 0.06, 0.054 for, Re_D=13400, Re_D=17500 at x/D_h =0.64, and x/D_h =0.46, respectively. In figure 4.20, the extreme value of Reynolds shear stress was found at x/D_h =0.43, and x/D_h =0.21 for Re_D=13400, Re_D=17500, respectively.

The Reynolds shear stress patterns of the bio-body differ from those of the cylinder. Bio-body consists of only two large-scale clusters in downstream. Well-defined Reynolds shear stress patterns indicate 75% lower Reynold stress in magnitude than the cylinder for Re_D= 13400.

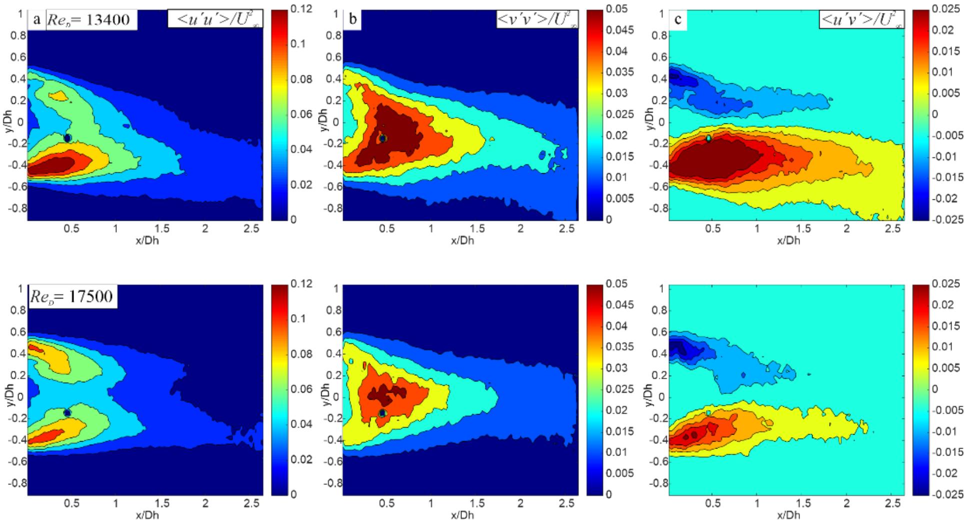

Figure 4.19. (a) streamwise Reynolds normal stresses $<u'u'>/U_\infty^2$ (b) transverse Reynolds normal stresses $<v'v'>/U_\infty^2$ (c) Reynolds shear stresses $<u'v'>/U_\infty^2$

5. CONCLUSION

This study aimed to design a new bio-body inspired by shark skin denticles to reduce the pressure drag by eliminating the shedding of vortices in bluff body wakes. In this regard, a novel body, called bio-body is created and the flow structures were compared with those of a circular cylinder which is one of the most studied bluff body geometry in the literature. The dimensions of the bio-body were determined according to dimensions of shark skin denticles reported by previous researches. Velocity field measurements were carried out in a water channel utilizing Particle Image Velocimetry (PIV) technique. Three different Reynolds numbers based on the hydraulic diameter were considered for the study; Re_D=4450, Re_D=8900 and Re_D=13400.

The results obtained from the circular cylinder were found to be in good agreement with the literature, hence the measurements were validated. Then the flow features of bio-body and the cylinder were compared with each other to reveal and interpret the fundamental flow characteristics that made the bio-body to be preferable over the cylinder. Vortex formation lengths were evaluated using the streamline topologies which resulted in narrower wake for the bio-body by having a decreased length of formed vortices. Up to 13% decrease in the vortex formation length was obtained for bio-body. Besides, the fluctuations in both streamwise and the transverse directions were found much to be reduced by in for bio-body compared with the circular cylinder. According to the lower fluctuations in the wake, it can be concluded that the bio-body might possess better aero-hydrodynamic characteristics than that of a circular cylinder (see Figure 4.10, 4.11, 4.13, 4.16, 4.19, 4.20). Moreover, the streamwise and transverse Reynolds normal stresses and Reynolds shear stress were evaluated to be lower for bio-body. The maximum reductions in normal and shear stresses were obtained for bio-body are 71.1%, 88.4%, and 77% for streamwise, transverse Reynolds normal stress, and Reynolds shear stresses, respectively. It is expected according to these results that the pressure drag exerted on the bio-body will also be significantly reduced compared with the other blunt body shapes.

Finally, the Fast Fourier Transformation technique were applied to obtain the possible shedding frequencies and/or any periodic events in the wake of both bio-body and cylinder. The calculated Strouhal number obtained for the cylinder was also in a good agreement with the theoretical value. However, no distinct peak was obtained for the bio-body revealing that in contrast to the cylinder results, the fluid flow downstream of the bio-body does not possess a periodic flow structure. This might be due to the tendency of boundary layer to stay attached on the surface of the bio body. Therefore, it can be concluded that the vortex shedding is eliminated by the generated bluff body which eventually eliminates the possible vortex-induced vibrations.

It is believed that this study contributes to the design and development of better aero/hydrodynamic geometries in various applications as also being a novel approach utilizing the biomimicry science. Measurements of drag force, three-dimensional velocity measurements and CFD simulations of this initial design can be performed as future studies which will enable to the enhancement for better streamlined shapes.

REFERENCES

Akilli, H., Karakus, C., Akar, A., Sahin, B., & Tumen, N. F. J. J. o. f. e. (2008). Control of vortex shedding of circular cylinder in shallow water flow using an attached splitter plate. *130*(4).

Aljure, D., Rodríguez, I., Lehmkuhl, O., Pérez-Segarra, C. D., Oliva, A. J. I. J. o. H., & Flow, F. (2015). Influence of rotation on the flow over a cylinder at Re= 5000. 55, 76-90.

Askew, G. N., & Marsh, R. L. J. J. o. E. B. (1997). The effects of length trajectory on the mechanical power output of mouse skeletal muscles. *200*(24), 3119-3131.

Basu, R. J. J. o. W. E., & Aerodynamics, I. (1985). Aerodynamic forces on structures of circular cross-section. Part 1. Model-scale data obtained under two-dimensional conditions in low-turbulence streams. 21(3), 273-294.

Basu, R. J. J. o. W. E., & Aerodynamics, I. (1986). Aerodynamic forces on structures of circular cross-section. Part 2. The influence of turbulence and three-dimensional effects. 24(1), 33-59.

Bechert, D., Bruse, M., Hage, W. v., Van der Hoeven, J. T., & Hoppe, G. J. J. o. f. m. (1997). Experiments on drag-reducing surfaces and their optimization with an adjustable geometry. *338*, 59-87.

Bechert, D., Bruse, M., Hage, W., & Meyer, R. J. N. (2000). Fluid mechanics of biological surfaces and their technological application. *87*(4), 157-171.

Bhushan, B. J. P. T. o. t. R. S. A. M., Physical, & Sciences, E. (2009). Biomimetics: lessons from nature–an overview. *367*(1893), 1445-1486.

Bodling, A., Sharma, A. J. J. o. S., & Vibration. (2019). Numerical investigation of noise reduction mechanisms in a bio-inspired airfoil. *453*, 314-327.

Cengel, Y. A. (2010). Fluid mechanics. Tata McGraw-Hill Education.

Choi, H., Jeon, W.-P., & Kim, J. J. A. R. F. M. (2008). Control of flow over a bluff body. 40, 113-139.

Derakhshandeh, J. F., & Alam, M. M. (2019). A review of bluff body wakes. Ocean Engineering, 182, 475-488.

Domel, A. G., Saadat, M., Weaver, J. C., Haj-Hariri, H., Bertoldi, K., & Lauder, G. V. J. J. o. t. R. S. I. (2018a). Shark skin-inspired designs that improve aerodynamic performance. *15*(139), 20170828.

Domel, A. G., Domel, G., Weaver, J. C., Saadat, M., Bertoldi, K., & Lauder, G. V. (2018b). Hydrodynamic properties of biomimetic shark skin: effect of denticle size and swimming speed. Bioinspiration & biomimetics, 13(5), 056014.Rostamy, N., Sumner, D., Bergstrom, D. J., & Bugg, J. D. (2012). Local flow field of a surface-mounted finite circular cylinder. Journal of Fluids and Structures, 34, 105-122.

Durhasan, T., Pinar, E., Ozkan, G., Aksoy, M., Akilli, H., & Sahin, B. J. E. J. o. M.-B. F. (2018). PIV measurement downstream of perforated cylinder in deep water. 72, 225-234.

Durhasan, T., Pinar, E., Ozkan, G., Akilli, H., & Sahin, B. J. A. O. R. (2019). The effect of shroud on vortex shedding mechanism of cylinder. 84, 51-61.

Fish, F., & Lauder, G. V. J. A. R. F. M. (2006). Passive and active flow control by swimming fishes and mammals. *38*, 193-224.

Gabbai, R., Benaroya, H. J. J. o. S., & Vibration. (2005). An overview of modeling and experiments of vortex-induced vibration of circular cylinders. 282(3-5), 575-616.

Garcia-Mayoral, R., & Jimenez, J. J. J. o. F. M. (2011). Hydrodynamic stability and breakdown of the viscous regime over riblets. *678*, 317.

Gim, O.-S., Kim, S.-H., & Lee, G.-W. J. O. e. (2011). Flow control behind a circular cylinder by control rods in uniform stream. 38(17-18), 2171-2184.

Griffin, O. M., & Ramberg, S. E. J. J. o. F. M. (1974). The vortex-street wakes of vibrating cylinders. *66*(3), 553-576.

Jordan, S. A. J. I. J. o. H., & Flow, F. (2002). Investigation of the cylinder separated shear-layer physics by large-eddy simulation. *23*(1), 1-12.

Katopes, D. Nikolas, Enviromental Fluid Mechanics (2019). *Free surface flow*, 324-426.

Keane, R. D., Adrian, R. J. J. M. s., & technology. (1990). Optimization of particle image velocimeters. I. Double pulsed systems. *1*(11), 1202.

Keane, R. D., Adrian, R. J. J. M. s., & technology. (1991). Optimization of particle image velocimeters: II. Multiple pulsed systems. *2*(10), 963.

KUMAR, S. M. J. J. o. S., & Vibration. (2001). FLOW-INDUCED VIBRATIONS OF A LIGHT CIRCULAR CYLINDER AT REYNOLDS NUMBERS 10^3 TO 10^4. *245*(5), 923-946.

LaVision. (2013) "DaVis Flowmaster Software Manual." LaVision GmbH, Goettingen, Germany.

LaVision. (2013) "DaVis 8.2 Software Manual." LaVision GmbH, Goettingen, Germany.

Lindken, R., & Burgmann, S. (2012). Laser-optical methods for transport studies in low temperature fuel cells. In Polymer electrolyte membrane and direct methanol fuel cell technology (pp. 425-461). Woodhead Publishing.

Lu, X.-Y., Sato, J. J. J. o. F., & Structures. (1996). A numerical study of flow past a rotationally oscillating circular cylinder. 10(8), 829-849.

Mayne, R., Patton, D., Costello, B. D., Adamatzky, A., & Patton, R. C. (2011). On the Internalisation, Intraplasmodial Carriage and Excretion of Metallic Nanoparticles in the Slime Mould, Physarum Polycephalum. International Journal of Nanotechnology and Molecular Computation (IJNMC), 3(3), 1-14.

Merrick, R., & Bitsuamlak, G.T. (2008). Control of flow around a circular cylinder by the use of surface roughness : A computational and experimental approach.

Motta, P., Habegger, M. L., Lang, A., Hueter, R., & Davis, J. J. J. o. m. (2012). Scale morphology and flexibility in the shortfin mako Isurus oxyrinchus and the blacktip shark Carcharhinus limbatus. *273*(10), 1096-1110.

Ozkan, G. M., Firat, E., & Akilli, H. J. O. E. (2017). Passive flow control in the near wake of a circular cylinder using attached permeable and inclined short plates. 134, 35-49.

Park, C. W., & Lee, S. J. (2000). Free end effects on the near wake flow structure behind a finite circular cylinder. Journal of Wind Engineering and Industrial Aerodynamics, *88*(2-3), 231-246.

Post, M. L., Decker, R., Sapell, A. R., Hart, J. S. J. A. S., & Technology. (2018). Effect of bio-inspired sinusoidal leading-edges on wings. *81*, 128-140.

Rodríguez, I., Lehmkuhl, O., Chiva, J., Borrell, R., Oliva, A. J. I. J. o. H., & Flow, F. (2015). On the flow past a circular cylinder from critical to super-critical Reynolds numbers: Wake topology and vortex shedding. 55, 91-103.

Sarpkaya, T. J. J. o. f., & structures. (2004). A critical review of the intrinsic nature of vortex-induced vibrations. 19(4), 389-447.

Shi, S.-x., Liu, Y.-z., & Chen, J.-m. J. J. o. H. (2012). An experimental study of flow around a bio-inspired airfoil at Reynolds number 2.0× 10 3. *24*(3), 410-419.

Sumner, D., Richards, M. D., & Akosile, O. O. (2005). Two staggered circular cylinders of equal diameter in cross-flow. Journal of Fluids and Structures, 20(2), 255-276.

Unal, M., & Rockwell, D. J. J. o. F. M. (1988). On vortex formation from a cylinder. Part 1. The initial instability. *190*, 491-512.

Unal, M., & Rockwell, D. J. J. o. F. M. (1988). On vortex formation from a cylinder. Part 2. Control by splitter-plate interference. 190, 513-529.

Wang, X., Chen, J., Zhou, B., Li, Y., & Xiang, Q. (2021). Experimental investigation of flow past a confined bluff body: Effects of body shape, blockage ratio and Reynolds number. Ocean Engineering, 220, 108412.

Wen, L., Weaver, J. C., Thornycroft, P. J., Lauder, G. V. J. B., & biomimetics. (2015). Hydrodynamic function of biomimetic shark skin: effect of denticle pattern and spacing. 10(6), 066010.

Westerweel, J., & Scarano, F. J. E. i. f. (2005). Universal outlier detection for PIV data. 39(6), 1096-1100.

Westerweel, J. J. M. s., & technology. (1997). Fundamentals of digital particle image velocimetry. *8*(12), 1379.

White, F. M. (1979). Fluid mechanics: Tata McGraw-Hill Education.

Williamson, C., & Govardhan, R. J. A. R. F. M. (2004). Vortex-induced vibrations. *36*, 413-455.

Williamson, C. H. J. A. r. o. f. m. (1996). Vortex dynamics in the cylinder wake. *28*(1), 477-539.

Zdravkovich, M. M. J. F. (1997). Flow around circular cylinders. *1*, 566-571.

CURRICULUM VITAE

He graduated from Güzelyurt Türk Maarif prep school in 2014 and enrolled in the Mechanical Engineering Department of Çukurova University in the same year. In 2018, he graduated with a Bachelor of Science degree in mechanical engineering.